

Non-LTE Models and Theoretical Spectra of Accretion Disks in Active Galactic Nuclei II. Vertical Structure of the Disk

Ivan Hubeny¹

AURA/NOAO, NASA Goddard Space Flight Center, Code 681, Greenbelt, MD 20771

and

Veronika Hubeny²

Department of Physics, University of California, Santa Barbara, CA 93106

Received _____; accepted _____

¹hubeny@tlusty.gsfc.nasa.gov

²veronika@physics.ucsb.edu

ABSTRACT

We have calculated several representative models of vertical structure of an accretion disk around a supermassive Kerr black hole. The interaction of radiation and matter is treated self-consistently, taking into account departures from LTE for calculating both the disk structure and the radiation field. The structural equations are described in detail, and various approximations are discussed. We have demonstrated that departures from LTE are very important for determining the disk structure, even at the midplane, as well as the emergent radiation, particularly for hot and electron-scattering-dominated disks. We have shown that at least for the disk parameters studied in this paper, NLTE effects tend to reduce the value of the Lyman jump with respect to the LTE predictions, regardless whether LTE predicts an emission or absorption jump. We have studied the effects of various values of viscosity on the model structure and predicted spectral energy distribution. The viscosity is parameterized through a parameter α_0 which describes the vertically-averaged viscous stress, two power-law exponents ζ_0 and ζ_1 , and the division point m_d between these two forms. The disk structure and emergent radiation is sensitive mainly to the values of α_0 , while the other parameters influence the disk structure to a much lesser extent. However, although the detailed shape of the predicted spectrum is sensitive to adopted value of α_0 , the overall appearance of the spectrum is quite similar.

Subject headings: accretion, accretion disks— galaxies:active—galaxies:nuclei—radiative transfer

1. INTRODUCTION

Accretion disks around massive black holes have long been the most popular candidates for providing the ultraviolet and soft X-ray flux observed in Active Galactic Nuclei (AGN). Observational evidence is mainly based on the ‘big blue bumps’ seen in the UV (e.g. Shields 1978; Malkan & Sargent 1982). However, despite its attractiveness this model faces a number of problems when confronted with multi-wavelength observations. The current situation has been recently summarized by Koratkar (1998) from the observational point of view, and by Blaes (1998) from the theoretical viewpoint. The most pressing problems of the theoretical models are a near absence of observed Lyman discontinuity (first pointed out by Antonucci, Kinney, & Ford 1989), the UV/EUV continuum polarization (e.g., Antonucci 1992, Blaes 1998 and references therein), the overall continuum spectral energy distribution (e.g. Laor 1990), and phased optical/UV variability (e.g., Alloin et al 1985).

What is clearly needed is a self-consistent model which would explain all the observed features. Such a goal is still far away, but we feel that the first step towards it is to answer the fundamental question: In view of all current problems, is the accretion disk paradigm still a viable model? In other words, are the observed phenomena truly inconsistent with the accretion disk picture in general, or is the lack of agreement rather a result of inaccuracies or even inconsistencies in the computed models or in the current modeling techniques?

Therefore, we have embarked on a systematic study of these questions. We recognize that there are many possible sources of inconsistencies in the AGN accretion disk modeling. There are essentially two types of problems. First, there are basic physical uncertainties. Among them, the most important is our ignorance of the basic physics of viscous energy dissipation in the AGN disks, so that we are left with a necessity to employ certain *ad hoc* parameters. Although this is certainly a viable approach when nothing else is currently available, we should bear in mind that corresponding models will lack predictive power—we may explain what we see, but we cannot predict it. In any case, when adopting a model based on some chosen set of parameters, one at least has to study carefully the influence of these parameters on the computed model. Other

fundamental physical problems are uncertainties of the effects of other structures forming the AGN complex onto the accretion disk; for instance an irradiation of the disk from external sources. Again, in the absence of any detailed theory, we are usually left with a necessity to parameterize these effects.

Second type of problems concerns the degree of approximation used in the actual modeling procedure. A particularly important class of such approximations deals with the description of interaction of radiation and matter in the disk. It should be emphasized that AGN disks, like atmospheres of hot stars, are typical examples of a medium where radiation is not only a *probe* of the physical state, but in fact a crucial *constituent*. In other words, radiation not only carries an information about the medium, it in fact *determines* its structure. Consequently, a treatment of this interaction is in a sense the very gist of the problem. We should therefore study the influence of various approximations, such as the degree of equilibrium assumed, or, more specifically, the extent to which the local thermodynamic equilibrium (LTE) applies, and the completeness of considered opacity and emissivity sources on the computed model, etc.

In the previous paper (Hubeny & Hubeny 1997 – hereafter called Paper I), we have presented some representative self-consistent, non-LTE models of the vertical structure of AGN accretion disks. The basic aim of that study was to investigate the differences in the predicted spectrum between this and previous approaches (Sun & Malkan 1989; Laor & Netzer, 1989; Ross, Fabian, & Mineshige 1992; Wehrse et al. 1993; Störzer and Haushildt 1994; Coleman 1994; Shields & Coleman 1994; Blaes & Agol 1996; Dörrer et al. 1996). The emphasis was to clarify the role of departures from LTE and to study the effects of simplifications of the hydrostatic equilibrium equation based on assuming a depth-independent vertical gravity acceleration.

In the present paper, we will consider models of vertical structure of AGN disks in detail. In particular, we will study the dependence of computed vertical structure and corresponding emergent spectrum on the adopted value of viscosity and on the degree of sophistication of the modeling procedure. In order to better emphasize the observable consequences of self-consistent, non-LTE models, we present the predicted spectra for a few representative points on the disk.

Complete spectra which are obtained by integrating the local spectra over the disk surface, taking into account general relativistic photon transfer functions (Cunningham 1975; Speith, Riffert, & Ruder 1995; Agol 1997; Agol, Hubeny, & Blaes 1998), will be considered in subsequent papers of this series.

Our aim here is not to construct a model to be used for comparison with actual observations. Instead, we intend to study the sensitivity of computed models on the degree of approximations used in the modeling procedure. Therefore, we will first give a detailed overview of the structural equations and the modeling procedures. This is meant to provide a firm framework on which our approach is based, which in turn is useful to assessing possible systematic effects within our models.

2. BASIC EQUATIONS AND APPROXIMATIONS

2.1. Relativistic Disk Structure

We assume a steady-state, thin, rotationally symmetric disk. We define the thin disk by the two conditions, namely *a*) the disk height, $h(R)$, at radial distance R is much smaller than R , i.e., $h(R) \ll R$, and *b*) all the components of the energy flux vector are negligible to that in the vertical direction, i.e., the direction perpendicular to the disk plane. Vertical distance from the disk plane is denoted z . We also assume the standard disk model, in which the azimuthal velocity is much larger than the radial velocity, and the vertical velocity component is neglected altogether.

The equations for relativistic disk structure were derived by Novikov & Thorne (1973), Page & Thorne (1974), Eardley & Lightman (1975) – who have corrected a previously incorrect term in the vertical pressure balance, and recently by Riffert & Herold (1996) whose results we use here.

The four basic equations describing the disk structure are:

i) *Vertical hydrostatic equilibrium,*

$$\frac{\partial P}{\partial z} = -\rho z \frac{GM}{R^3} \frac{C}{B}, \quad (1)$$

where P is the total pressure, ρ is the mass density, G is the gravitational constant, M is the black hole mass, and B and C (together with A and D used later) are the so-called relativistic corrections – see below. We note that Abramowicz, Lanza, & Percival (1997) have recently rederived the vertical hydrostatic equilibrium equation, and showed that previous treatments yielded some unphysical singularities close to the last stable orbit.

ii) *Energy balance equation*,

$$\frac{\partial F_z}{\partial z} = \frac{3}{2} \sqrt{\frac{GM}{R^3}} \frac{A}{B} t_{\phi r}, \quad (2)$$

where F_z is the z -component of the energy flux, and $t_{\phi r}$ is the sheer stress (also called the viscous stress).

iii) *Azimuthal momentum balance* (written using the equation of continuity, and with the boundary condition $t_{\phi r} = 0$ at the innermost stable orbit),

$$\int_{-h}^h t_{\phi r} dz = \frac{\dot{M}}{2\pi} \sqrt{\frac{GM}{R^3}} \frac{D}{A}, \quad (3)$$

where \dot{M} is the mass accretion rate.

iv) Finally, the *equation describing the source of viscous stress*,

$$t_{\phi r} = \frac{3}{2} \eta \sqrt{\frac{GM}{R^3}} \frac{A}{B}, \quad (4)$$

which specifies the viscous stress in terms of velocity gradients and the sheer viscosity, η .

The relativistic corrections are given by

$$A = 1 - \frac{2}{r} + \frac{a^2}{r^2}, \quad (5)$$

$$B = 1 - \frac{3}{r} + \frac{2a}{r^{3/2}}, \quad (6)$$

$$C = 1 - \frac{4a}{r^{3/2}} + \frac{3a^2}{r^2}, \quad (7)$$

$$D = \frac{1}{2\sqrt{r}} \int_{r_i}^r \frac{x^2 - 6x + 8a\sqrt{x} - 3a^2}{\sqrt{x}(x^2 - 3x + 2a\sqrt{x})} dx, \quad (8)$$

where r is radius of the annulus expressed in units of the gravitational radius, $R_g = GM/c^2$, i.e., $r = R/(GM/c^2)$; and the specific angular momentum a/M is expressed in units of G/c ; c being the speed of light, and r_i the radius of the innermost stable orbit.

Equations (1) - (4) are general equations which describe the structure of the disk. To make them applicable to real disks, one has to specify, in addition, *a*) the nature of the energy flux (i.e. how the energy generated by viscous shear is transported), and *b*) the nature (and numerical value) of the shear viscosity.

The first item is straightforward. It is usually assumed that the energy is transported solely by radiation (plus possibly in part by convection in convectively unstable layers). In this case F_z is the total radiation flux. From Eq. (2) it follows that

$$F_z(z=h) = \frac{3}{2} \sqrt{\frac{GM}{R^3}} \frac{A}{B} \int_0^h t_{\phi r} dz, \quad (9)$$

because the flux vanishes at the disk plane, $F_z(z=0) = 0$, since the disk is symmetric about the disk midplane. It is customary to express the total energy flux at the disk surface through the *effective temperature*. As follows from Eqs. (9) and (3),

$$F_z(z=h) \equiv \sigma T_{\text{eff}}^4 = \frac{3}{8\pi} \frac{GM\dot{M}}{R^3} \frac{D}{B}, \quad (10)$$

where σ is the Stefan–Boltzmann constant. The effective temperature has thus the meaning of the temperature for which the corresponding black-body radiation has the total radiation energy (integrated over all frequencies) equal to the total energy generated in the column of unit cross-section in the disk. This explains why the early approaches used the black-body radiation for describing the disk radiation; however, we stress that the radiation emergent from the disk does not have to possess the black-body frequency distribution.

2.2. Viscosity

Viscosity is the most uncertain physical quantity of the accretion disk modeling. There is no theory that would explain the accretion disk viscosity from first principles, although, at least in

the case of accretion disks in the cataclysmic variables, the Balbus–Hawley (1991) instability and subsequent detailed numerical MHD simulations (e.g., Stone et al. 1996) represent a breakthrough in our understanding of disk viscosity, and offer a great promise for the future.

In this paper, we adopt the traditional approach, and parameterize the viscosity by means of some adjustable parameters. First, we express the sheer viscosity through the *kinematic viscosity*, w , as

$$\eta \equiv \rho w. \quad (11)$$

We also introduce the *vertically averaged kinematic viscosity*,

$$\overline{w} = \frac{\int_0^h w \rho dz}{\int_0^h \rho dz} = \frac{1}{m_0} \int_0^h \eta dz = \frac{1}{m_0} \int_0^{m_0} w dm, \quad (12)$$

where we have introduced the column mass, $dm = -\rho dz$, i.e., $m(z)$ is the column mass above the height z . The total column density at the disk midplane is denoted by m_0 , and is related to the traditional disk surface density, Σ , by $m_0 = \Sigma/2$.

The most commonly used viscosity parameterization is the so-called α -prescription (Shakura & Sunyaev 1973). In this model, viscosity is thought to be caused by turbulence; the kinematic viscosity is then postulated, by a simple dimensional analysis, to be equal to

$$w = \alpha l_{\text{turb}} v_{\text{turb}}, \quad (13)$$

where l_{turb} and v_{turb} are the size and velocity of the largest turbulent cells, respectively, and α is an ad hoc proportionality constant. There are several variants of the α -prescription, depending of what is taken for l_{turb} and v_{turb} . Typically, l_{turb} is taken to be equal to h , the disk height, and v_{turb} equal to the sound speed, $c_s = \sqrt{(P/\rho)}$, or some other turbulent velocity. This is a *local* description. In fact, the original Shakura-Sunyaev α was introduced to describe *vertically-averaged* quantities, and we use this description here as well. We define

$$\overline{t_{\phi r}} \equiv \frac{1}{h} \int_0^h t_{\phi r} dz = \alpha_0 \overline{P}, \quad (14)$$

where \overline{P} is the vertically-averaged total pressure. Further, we write

$$\int_0^h t_{\phi r} dz = h \alpha_0 \overline{P} = m_0 \alpha_0 (\overline{P}/\overline{\rho}), \quad (15)$$

where $\bar{\rho} = m_0/h$ is the vertically averaged density.

In this paper, we do not consider \bar{P} and $\bar{\rho}$ to be the model-dependent averages of actual pressure and density. Instead, the factor $(\bar{P}/\bar{\rho})$ is taken as a known function of the basic parameters of the disk and the radius of the annulus, having the value corresponding to the case of radiation-pressure-dominated disks, $(\bar{P}/\bar{\rho}) = (\bar{P}/\bar{\rho})_{\text{rad}}$. This value is given by (see Sect 3.1 for a detailed derivation)

$$\frac{\bar{P}}{\bar{\rho}} = \frac{3GM\dot{M}}{R^3} \left(\frac{\sigma_e}{8\pi m_H c} \right)^2 \frac{D^2}{BC}, \quad (16)$$

where σ_e is the electron (Thomson) scattering cross-section, and m_H is the mass of hydrogen atom. The vertically averaged kinematic viscosity then follows from integrating Eq. (4) over z , and using Eqs. (12), (15) and (16),

$$\bar{w} = 2\dot{M}^2\alpha_0 \sqrt{\frac{GM}{R^3}} \left(\frac{\sigma_e}{8\pi m_H c} \right)^2 \frac{D^2}{AC}. \quad (17)$$

The advantage of this parameterization of viscosity is that it yields the total column mass as an explicit function of radial distance. Substituting Eqs. (15) and (16) into (3), we obtain

$$m_0 = \frac{16\pi}{3} \left(\frac{m_H c}{\sigma_e} \right)^2 \sqrt{\frac{R^3}{GM}} \frac{1}{\dot{M}\alpha_0} \frac{BC}{AD}. \quad (18)$$

Because of this feature, we can easily use the mass column density, m , as an independent depth variable of the problem. This has a significant benefit of greater numerical stability of the solution of the structural equations, in particular the radiative transfer and the hydrostatic equilibrium equations – see below.

Alternatively, one may parameterize the vertically-averaged kinematic viscosity through the Reynolds number, Re , which is an approach suggested already by Lynden-Bell & Pringle (1974),

$$\bar{w} = \frac{\sqrt{GMR}}{Re}, \quad (19)$$

in which case

$$m_0 = \frac{\dot{M} Re}{6\pi\sqrt{GMR}} \frac{BD}{A^2}, \quad (20)$$

which follows directly from Eqs. (3) and (19). The relation between α_0 and Re follows from Eqs. (19) and (17),

$$Re = 2 \left(\frac{4\pi m_H c}{\sigma_e} \right)^2 \left(\frac{R}{\dot{M}} \right)^2 \frac{1}{\alpha_0} \frac{AC}{D^2}, \quad (21)$$

The (depth-dependent) viscosity w is allowed to vary as a step-wise power law of the mass column density, viz.

$$w(m) = w_0 (m/m_0)^{\zeta_0}, \quad m > m_d, \quad (22)$$

$$w(m) = w_1 (m/m_0)^{\zeta_1}, \quad m < m_d, \quad (23)$$

where m_d is the division point. In other words, we allow for a different power-law exponent for inner and outer layers. This represents a generalization of an approach we used previously, based on a single power-law representation introduced by Kříž & Hubeny (1986). The reason for choosing a two-step power law is that with a single power law we typically obtain a density inversion in the deep layers, while the main reason for introducing the power-law representation of viscosity in the first place was to prevent the “thermal catastrophe” of the disk in the low optical depth regions where the cooling due to strong resonance lines of light metals is important (see, e.g., Shaviv & Wehrse 1986; Hubeny 1990a). On the other hand, recent numerical simulations (Stone et al. 1996) indicate that the viscosity actually increases towards the surface, giving rise to a high-temperature region (corona) on the top of a disk. Such models were considered for instance by Sincell & Krolik (1997). We plan to study such non-standard models in future papers of this series; in this paper we will consider models where the viscosity decreases in the outer layers.

We have thus four independent parameters: exponents ζ_0 and ζ_1 , the division point, m_d , and the fraction, f , of energy dissipated in deep layers, $m > m_d$. The coefficients w_0 and w_1 are derived from the condition on the vertically averaged viscosity, $\int_0^{m_0} w(m) dm / m_0 = \bar{w}$, and $\int_{m_d}^{m_0} w(m) dm / m_0 = f \bar{w}$. We obtain

$$w_0 = \frac{f \bar{w}(\zeta_0 + 1)}{1 - (m_d/m_0)^{\zeta_0 + 1}}, \quad (24)$$

$$w_1 = \frac{(1-f) \bar{w}(\zeta_1 + 1)}{(m_d/m_0)^{\zeta_1 + 1}}. \quad (25)$$

Generally, $w(m)$ does not have to be continuous at the division point m_d . If we require the continuity, then f and m_d are no longer two independent parameters; instead, they are related through

$$\frac{m_d}{m_0} = \left(1 + \frac{\zeta_0 + 1}{\zeta_1 + 1} \frac{f}{1 - f} \right)^{-\frac{1}{\zeta_0 + 1}}. \quad (26)$$

Typically, the deep-layer power law exponent ζ_0 is set to 0 (constant viscosity), while the “surface” power law exponent ζ_1 is usually set to a value larger than zero. In §3.3, we will compare this treatment to a purely local α -parameterization of viscosity.

2.3. Equations for the Vertical Structure

Due to the assumption of thin disk, we may reduce a general 2-D problem of computing disk structure to a set of 1-D problems. The disk is divided into a set of axially symmetric concentric annuli; each annulus behaves as a one-dimensional radiating slab. The vertical structure of a single annulus is computed by solving simultaneously the hydrostatic equilibrium equation, the energy balance equation, the radiative transfer equation, and, since we do not generally assume LTE, the set of statistical equilibrium equations. Below, we specify these equations in detail. Since the state parameters now depend only on the vertical distance z , we replace partial derivatives in Eqs. (1) and (2) by ordinary derivatives. Moreover, we take the column density m as the basic depth variable, as it is customary in modeling stellar atmospheres and non-relativistic accretion disks. Furthermore, we write down the terms corresponding to radiation (i.e., radiation pressure, and radiation flux) explicitly, to stress that we treat the radiation essentially exactly, without any simplifying assumptions about radiative transfer. Since the radiation terms in the structural equations are written using the radiative transfer equation, we start with it.

a) Radiative Transfer Equation

The radiative transfer equation is written in the standard way (e.g. Mihalas 1978), viz

$$\mu \frac{dI_\nu(\mu)}{d\tau_\nu} = I_\nu - S_\nu, \quad \text{or} \quad \mu \frac{dI_\nu(\mu)}{dm} = -\frac{1}{\rho} (\chi_\nu I_\nu - \eta_\nu), \quad (27)$$

where $I_\nu(\mu)$ is the specific intensity of radiation at frequency ν , μ being the cosine of the angle between direction of propagation and the normal to the disk midplane. The monochromatic optical depth is defined through $d\tau_\nu \equiv -\chi_\nu dz = (\chi_\nu/\rho)dm$; and the source function by $S_\nu \equiv \eta_\nu/\chi_\nu$. Here, χ_ν is the total absorption coefficient, $\chi_\nu = \kappa_\nu + \sigma_\nu$, σ_ν being the scattering coefficient. We assume that the only scattering process is the electron (Thomson) scattering, $\sigma_\nu = \sigma_e$; σ_e being the Thomson cross-section. Finally, η_ν is the emission coefficient, given by $\eta_\nu = \eta_\nu^{\text{th}} + \sigma_\nu J_\nu$, where η_ν^{th} is the coefficient of thermal emission. We assume the symmetry condition at the disk midplane, $I_\nu(\mu) = I_\nu(-\mu)$. The upper boundary condition is $I_\nu(\mu) = I_\nu^-, \mu < 0$, where I^- is a prescribed incident radiation. In the present paper we assume, for simplicity, the case of no external irradiation, $I^- = 0$. We return to the problem of non-zero external irradiation in a future paper of this series.

The first two moment equations of the transfer equation read

$$\frac{dH_\nu}{dm} = -\frac{1}{\rho} (\kappa_\nu J_\nu - \eta_\nu), \quad (28)$$

$$\frac{dK_\nu}{dm} = -\frac{\chi_\nu}{\rho} H_\nu, \quad (29)$$

where the moments of the specific intensity are defined by

$$[J_\nu, H_\nu, K_\nu] = \frac{1}{2} \int_{-1}^1 [1, \mu, \mu^2] I_\nu(\mu) d\mu, \quad (30)$$

We stress that in Eq. (28) the scattering terms cancel, so that the equation contains the true absorption coefficient κ_ν , instead of the total absorption coefficient χ_ν . The radiation flux is given by

$$F_{\text{rad}} = 4\pi \int_0^\infty H_\nu d\nu. \quad (31)$$

To solve the radiative transfer equation, we employ the Variable Eddington Factors technique (Auer & Mihalas 1970), which consists in introducing the Eddington factor $f_\nu^K = K_\nu/J_\nu$, and writing the transfer equation (27) as

$$\frac{d^2(f_\nu^K J_\nu)}{d\tau_\nu^2} = J_\nu - S_\nu. \quad (32)$$

This equation involves only the mean intensity of radiation, J_ν , which is a function of only frequency and depth, and not the specific intensity which in addition is a function of angle μ . Such an approach is extremely advantageous in methods which solve the global system of structural equations iteratively. The Eddington factor is determined by a set of frequency-by-frequency formal solutions of the transfer equation, and is held fixed at a subsequent iteration step of the global scheme.

b) Hydrostatic Equilibrium

The hydrostatic equilibrium equation reads, neglecting self-gravity of the disk and assuming that the radial distance from the black hole, R , is much larger than the vertical distance from the central plane, z ,

$$\frac{dP}{dm} = g(z), \quad (33)$$

where the depth-dependent vertical gravity acceleration is given by

$$g(z) = \frac{GM}{R^3} \frac{C}{B} z. \quad (34)$$

The total pressure is given as a sum of the gas pressure and the radiation pressure,

$$P = P_{\text{gas}} + P_{\text{rad}} = NkT + \frac{4\pi}{c} \int_0^\infty K_\nu d\nu, \quad (35)$$

where N is the total particle number density, T the temperature, k the Boltzmann constant. The upper boundary condition is taken from Hubeny (1990a – Eqs. 4.19–4.20 there).

c) Energy Balance

Substituting Eqs. (4) and (11) into (2), and using Eqs. (31) and (28), we obtain

$$\frac{9}{4} \frac{GM}{R^3} \left(\frac{A}{B} \right)^2 \rho w = 4\pi \int_0^\infty (\eta_\nu - \kappa_\nu J_\nu) d\nu. \quad (36)$$

The energy balance equation may be cast to different form if we do not express the radiation flux through the moment equation of the transfer equation, namely

$$\frac{dF_{\text{rad}}}{dm} = -\frac{9}{4} \frac{GM}{R^3} \left(\frac{A}{B} \right)^2 w(m). \quad (37)$$

Since the radiation flux at the midplane, $m = m_0$, is zero, equation (37) may be integrated to yield

$$F_{\text{rad}}(m) = \frac{9}{4} \frac{GM}{R^3} \left(\frac{A}{B} \right)^2 \int_m^{m_0} w(m') dm'. \quad (38)$$

Using Eqs. (12) – (20), and the definition of effective temperature, Eq. (10), we obtain finally

$$F_{\text{rad}}(m) = \sigma T_{\text{eff}}^4 [1 - \theta(m)], \quad (39)$$

where the auxiliary function θ is defined by

$$\theta(m) = \frac{1}{\bar{w} m_0} \int_0^m w(m') dm'. \quad (40)$$

For any depth dependence of viscosity, θ is a monotonically increasing function of m , between $\theta(0) = 0$, and $\theta(m_0) = 1$. For a depth-independent viscosity, $\theta(m) = m/m_0$, and for the adopted step-wise power law defined by Eqs. (22) – (26), it is given by

$$\theta(m) = (1 - f) (m/m_d)^{\zeta_1+1}, \quad m \leq m_d, \quad (41)$$

$$\theta(m) = (1 - f) + f \frac{(m/m_0)^{\zeta_0+1} - (m_d/m_0)^{\zeta_0+1}}{1 - (m_d/m_0)^{\zeta_0+1}}, \quad m \geq m_d. \quad (42)$$

d) The z – m relation

Since the hydrostatic equilibrium equation (33) contains the vertical distance z explicitly, we have to supply the relation between z and m , which reads simply

$$\frac{dz}{dm} = -\frac{1}{\rho}. \quad (43)$$

e) Absorption and emission coefficient

The absorption coefficient is given by

$$\begin{aligned} \chi_\nu &= \sum_i \sum_{j>i} [n_i - (g_i/g_j)n_j] \sigma_{ij}(\nu) + \sum_i \left(n_i - n_i^* e^{-h\nu/kT} \right) \sigma_{i\kappa}(\nu) \\ &\quad + \sum_\kappa n_e n_\kappa \sigma_{\kappa\kappa}(\nu, T) \left(1 - e^{-h\nu/kT} \right) + n_e \sigma_e, \end{aligned} \quad (44)$$

where n_i is the number density (population) of an energy level i (we number all levels consecutively, without notational distinction of the parent atom and ion), n_i^* the corresponding LTE population,

g_i the statistical weight, and $\sigma(\nu)$ the appropriate cross-section. The four terms represent, respectively, the contributions of bound-bound transitions (i.e. spectral lines), bound-free transitions (continua), free-free absorption (inverse brehmstrahlung), and of electron scattering. Subscript κ denotes the “continuum”, and n_κ the ion number density. The negative contributions in the first three terms represent the stimulated emission. There is no stimulated emission correction for the scattering term, since this contribution cancels with ordinary absorption for coherent scattering (for an illuminating discussion, see Shu 1991).

Analogously, the thermal emission coefficient is given by

$$\begin{aligned} \eta_\nu^{\text{th}} = & \left(2h\nu^3/c^2\right) \left[\sum_i \sum_{j>i} n_j (g_i/g_j) \sigma_{ij}(\nu) + \sum_i n_i^* \sigma_{i\kappa}(\nu) e^{-h\nu/kT} \right. \\ & \left. + \sum_\kappa n_e n_\kappa \sigma_{\kappa\kappa}(\nu, T) e^{-h\nu/kT} \right]. \end{aligned} \quad (45)$$

The three terms again describe the bound-bound, bound-free, and free-free emission processes, respectively.

These equations should be complemented by expressions for the relevant cross-sections, definition of LTE populations, and other necessary expressions.

We did not yet implement the Compton scattering in our codes, but the work on this problem is under way, and will be reported in a future paper. Nevertheless, Compton scattering is not important for the models considered in this paper, as we shall verify in Sect. 3.1.

f) Statistical Equilibrium Equation

It is well known that the LTE approximation breaks down in low-density, radiation-dominated media (see, e.g. Mihalas 1978), which are precisely the conditions prevailing in the AGN disks. Therefore, we have to adopt a more general treatment, traditionally called non-LTE (or NLTE), where the populations of some selected energy levels of some selected atoms/ions are allowed to depart from the Boltzmann-Saha distribution. These populations are determined through the equations of statistical equilibrium (e.g. Mihalas 1978), viz.

$$n_i \sum_{j \neq i} (R_{ij} + C_{ij}) = \sum_{j \neq i} n_j (R_{ji} + C_{ji}) , \quad (46)$$

where R_{ij} and C_{ij} is the radiative and collisional rates, respectively, for the transition from level i to level j . The l.h.s. of (46) represents the total number of transitions out of level i , while the r.h.s. represents the total number of transitions into level i from all other levels. An essential numerical complication inherent to this approach is that the radiative rates are given as integrals over the radiation intensity, i.e., schematically

$$R_{ij} = \int_0^\infty (h\nu/4\pi) \sigma_{ij}(\nu) J_\nu d\nu. \quad (47)$$

2.4. Numerical Method

The overall system of Eqs. (32), (33), (36), (43), and (46), together with auxiliary expressions (34), (19) – (26), and the definition expressions for the absorption and emission coefficients, (44) and (45), form a highly coupled, non-linear set of integro-differential equations. Fortunately, these equations are very similar to the equations describing classical NLTE stellar atmospheres (see, e.g., Hubeny 1990a,b), where the modeling techniques are highly advanced. We may therefore employ to great advantage numerical methods and computer programs designed originally for stellar atmospheres.

We use here the computer program TLUSDISK, which is a derivative of the stellar atmosphere program TLUSTY (Hubeny 1988). The program is based on the hybrid complete-linearization/accelerated lambda iteration (CL/ALI) method (Hubeny & Lanz 1995). The method resembles the traditional complete linearization, however the radiation intensity in most (but not necessarily all) frequencies is not linearized; instead it is treated via the ALI scheme (for a review of the ALI method, see e.g., Hubeny 1992). A NLTE model of a vertical structure of one annulus of a disk is generally computed in several steps. First, an LTE-gray model is constructed, as described in Hubeny (1990a). This serves as the starting solution for the subsequent step, an LTE model, computed by TLUSDISK. This in turn is used as the starting solution for the next step, a NLTE model.

In the NLTE step, we first calculate the so-called NLTE/C model (i.e., NLTE with continua

only), assuming that all bound-bound transitions are in detailed radiative balance. Finally, in the last step, we consider all lines – we denote this model as NLTE/L. The lines influence the disk structure both directly – through their contribution to the total heating/cooling rate and to the total radiation pressure, as well as indirectly – through their influence on atomic level population via equations of statistical equilibrium. Therefore, they influence the heating/cooling rates and the radiation pressure in the continuum processes as well. However, one should be aware that considering lines is not, strictly speaking, consistent with the 1-D approach adopted here. The assumption of horizontally homogeneous rings implies that the Keplerian velocity is assumed constant within the ring. This is a good approximation for continua, but may be inaccurate for the radiation transfer in spectral lines because a difference of projected Keplerian velocity as small as the thermal velocity already shifts the line photon out of the Doppler core. The photon escape probability from a disk ring may therefore be quite different compared to the escape probability from a plane-parallel, static atmosphere. For a proper treatment of this problems we would have to abandon a 1-D modeling and construct a fully 2-D model. However, at present, we intend to explore a magnitude of various phenomena and their effect on the disk structure; we feel that for such an exploratory model study the 1-D treatment as described above is satisfactory.

3. SENSITIVITY ANALYSIS

As a representative case, we take a disk around a Kerr supermassive black hole with $M = 2 \times 10^9 M_\odot$, with the maximum stable rotation (the specific angular momentum $a/M = 0.998$). The mass flux is taken $\dot{M} = 1 M_\odot/\text{year}$. We have calculated a number of vertical structure models at various radii; we present here three representative models for $r = 2, 11$, and 20 . The corresponding effective temperature is (roughly) 80,000 K, 27,000 K, and 18,000 K, respectively; the models thus cover a representative range of effective temperatures of the AGN disk annuli.

For simplicity, we consider disks composed of hydrogen and helium only. This allows us to study various effects without spending too much computer time, while taking into account all

the essential physics. The effects of heavy elements on disk models will be considered in the subsequent paper. Here, we intend to investigate two questions, namely, i) the effect of degree of sophistication in the disk modeling (LTE versus NLTE; effects of lines); and ii) the sensitivity of computed model structure on the individual viscosity parameters.

Hydrogen is represented essentially exactly: The first 8 levels are treated separately, while the upper levels are merged into the averaged non-LTE level accounting for level dissolution as described by Hubeny, Hummer, & Lanz (1994). Neutral helium is represented by a 14-level model atom, which incorporates all singlet and triplet levels up to $n = 8$. The 5 lowest levels are included individually; singlet and triplet levels are grouped separately from $n = 3$ to $n = 5$, and we have formed three superlevels for $n = 6, 7$, and 8 . The first 14 levels of He^+ are explicitly treated. We assume a solar helium abundance, $N(\text{He})/N(\text{H}) = 0.1$.

In the NLTE/L models, all the lines are treated explicitly, assuming Doppler profiles with turbulent velocity ranging from the thermal velocity up to the vertically-averaged sound speed,

$$v_{\text{turb}} = \sqrt{\overline{P}/\overline{\rho}}, \quad (48)$$

where $(\overline{P}/\overline{\rho})$ is given by Eq. (16). For the three annuli at $r = 2, 11$, and 20 , of the disk specified above, the sound speed has values of $3880, 770$, and 375 km s^{-1} , respectively. Although considering different values of v_{turb} has a significant effect on computed rest-frame line profiles, we found a negligible effect on the resulting disk structure.

3.1. Non-LTE Effects

Figure 1 shows the temperature as a function of depth for the three annuli. The depth is expressed as column mass in g cm^{-2} . We see several interesting features. Firstly, for the hot model at $r = 2$ ($T_{\text{eff}} = 80,000 \text{ K}$), the NLTE temperature structure differs appreciably from the LTE structure, even at the midplane. The cooler models exhibit different temperature at the upper layers, i.e. for $\log m \lesssim 1.5$, while the temperature structure is unchanged by NLTE effects

in the deep layers. This is explained by the fact that the effective optical thickness

$$\tau_{\text{eff}} \approx \sqrt{\tau_{\text{tot}} \tau_{\text{abs}}},$$

(where τ_{tot} is the total optical depth corresponding to χ , i.e., including electron scattering, while τ_{abs} is the optical depth corresponding to the true absorption, κ), becomes comparable to or smaller than 1 for hot models. In other words, a photon created at the midplane has a non-zero probability that it will undergo a series of consecutive scatterings without being destroyed by a thermal process until it escapes from the disk surface. Consequently, even the deep layers of the disk now effectively “feel” the presence of the boundary, which gives rise to NLTE effects even close to the midplane.

Secondly, as expected, differences between NLTE/C and NLTE/L models are negligible in the deep layers, while they are important in the upper layers – the lines heat up the upper disk atmosphere (for $\log m \lesssim 0.5$) by some 10,000 K for the hot model; by 4,000 K for the intermediate ($r = 11$) model, and by only 1000 K for the “cool” model. The effect is exactly analogous to the temperature rise predicted in hot stellar atmospheres (Mihalas 1978), which is explained as an indirect effect of Lyman and Balmer lines on the heating in the Lyman and Balmer continuum. The explanation goes as follows: roughly speaking, the temperature structure is determined by the balance between the radiative heating, which is mostly provided by the Lyman (for hotter models) and the Balmer (for cooler models) continuum, and the radiation cooling in the free-free transitions in the optical and infrared region. Radiative transfer in the Lyman (Balmer) lines explicitly gives rise to an overpopulation of the hydrogen $n = 1$ ($n = 2$) states, which leads to an increase of the efficiency of the Lyman (Balmer) continua which in turn leads to an additional heating at the surface. There is a competition between this heating and the traditional surface cooling caused by the lines, but in the present case the indirect effect dominates.

In Fig. 2, we plot the density structure for the same models as displayed in Fig. 1. For the hot model, density is almost unaffected by NLTE effects. This is easy to understand, since in this case the radiation pressure is completely dominant, and the disk structure is given by the following

simple analytic formulae. The hydrostatic equilibrium equation (33) reduces to

$$\frac{dP_{\text{rad}}}{dm} = Q z, \quad (49)$$

where we have denoted $Q = (GM/R^3)(C/B)$. Using Eq. (35) and the first moment of the transfer equation, (29), we may express the gradient of the radiation pressure as

$$\frac{dP_{\text{rad}}}{dm} = \frac{4\pi}{c} \int_0^\infty \frac{dK_\nu}{dm} d\nu = \frac{4\pi}{c} \int_0^\infty \frac{\chi_\nu}{\rho} H_\nu d\nu = \frac{4\pi}{c} \chi_H H, \quad (50)$$

where χ_H is the flux-mean opacity, defined by

$$\chi_H = \int_0^\infty (\chi_\nu / \rho) H_\nu d\nu / H, \quad (51)$$

and H is the total (frequency-integrated) Eddington flux, $H = \int_0^\infty H_\nu d\nu = 4\pi F_{\text{rad}}$. The flux-mean opacity is particularly simple in the case when the electron scattering is the dominant source of opacity. In this case $\chi_H = n_e \sigma_e / \rho$. For a medium where hydrogen is fully ionized and helium is partially doubly ionized, the flux-mean opacity is given by $\chi_H = (\sigma_e / m_H)(1 + \alpha Y) / (1 + 4Y) \approx 0.4(1 + \alpha Y) / (1 + 4Y)$, where Y is the helium abundance, $Y = N(\text{He}) / N(\text{H})$, and $\alpha = 1 + N(\text{He}^{++}) / N(\text{He})$; m_H is the mass of hydrogen atom.

Using Eq. (39), we obtain

$$\frac{\sigma \chi_H}{c} T_{\text{eff}}^4 [1 - \theta(m)] = Q z. \quad (52)$$

We know that at the disk surface, $m = 0$, $\theta(m) = 0$, and therefore the total disk height, h , is given by

$$h = \frac{\sigma T_{\text{eff}}^4 \chi_H}{Q} \frac{c}{c} = \frac{3 \dot{M} \chi_H D}{8\pi c C}. \quad (53)$$

The hydrostatic equilibrium equation thus reduces to

$$\frac{z}{h} = 1 - \theta(m) \quad (54)$$

This equation enables us to estimate the density, since from Eq. (43) we know that $1/\rho = -dz/dm$, so that from Eq. (54) we obtain $1/\rho = h(d\theta/dm)$. However, from the definition of θ , Eq. (40) we have $d\theta/dm = w(m) / (\bar{w} m_0)$, so that we finally obtain

$$\rho(m) = \frac{m_0}{h} \frac{\bar{w}}{w(m)}. \quad (55)$$

This equation shows that the density structure for the case of dominant radiation pressure is solely determined by the dependence of viscosity on depth. For a depth-independent viscosity, density is constant, and is given by $\rho = m_0/h$, i.e the total column mass divided by the disk height.

Before proceeding further, we derive the term $(\bar{P}/\bar{\rho})$ for the case of radiation-pressure dominated disks. Assuming a depth-independent viscosity, the density is also constant, $\rho = \bar{\rho}$. The hydrostatic equilibrium equation thus reads $dP/dz = -Q\bar{\rho}z$, which has solution $P(z) = Q\bar{\rho}(h^2 - z^2)/2$, and consequently $\bar{P} = Q\bar{\rho}h^2/3$. Substituting for h from Eq. (53), we finally obtain

$$\frac{\bar{P}}{\bar{\rho}} = \frac{3GM\dot{M}}{R^3} \left(\frac{\chi_H}{8\pi m_H c} \right)^2 \frac{D^2}{BC}. \quad (56)$$

Substituting the pure-hydrogen form of χ_H , $\chi_H = \sigma_e/m_H$ into Eq. (56), we obtain Eq. (16) used in the definition of α_0 .

It should be stressed that Eqs. (49) through (55) apply if the *gradient* of the radiation pressure dominates over the gradient of the gas pressure, $dP_{\text{rad}}/dm \gg dP_{\text{gas}}/dm$; it is not sufficient that $P_{\text{rad}} \gg P_{\text{gas}}$. It is clear that even in the case where the radiation pressure dominates everywhere in the atmosphere, the radiation pressure gradient becomes very small in the upper layers where the optical depth is smaller than unity, because the radiation field is already formed and does not change when going outward. The gas pressure gradient then takes over in these layers, and consequently density starts to decrease exponentially with height. For a comprehensive discussion, see Hubeny (1990a).

In any case, Eq. (55) shows that in the inner layers of the radiation-pressure-dominated disks, density structure does depend only on viscosity, and is therefore insensitive to NLTE effects. This is indeed demonstrated in Fig. 2. The above considerations also explain that for the radiation-pressure-dominated disks the disk height depends only on the radial distance R , through the relativistic correction D/C , and slightly through χ_H (because of variations in the ionization of helium). The z - m relation is given through the depth dependence of viscosity, and is thus insensitive to local temperature, as well as to NLTE effects. This is demonstrated in Fig. 3, where we plot the vertical distance z as a function of m for the same models as displayed in Fig. 1.

Figure 4a displays the departure coefficient (*b*-factor) for the ground state of hydrogen for the three annuli, and for NLTE/C and NLTE/L models. Departure coefficient is defined as $b_i = n_i/n_i^*$. Near the midplane of the disk, the *b*-factor is close to unity because the optical depth is large. It starts to deviate from unity as soon as the Lyman continuum becomes effectively optically thin. The behavior of the hot model differs from the two cooler ones.

In the hot model, electron scattering dominates the opacity even in the Lyman continuum; the thermal coupling parameter

$$\epsilon_\nu = \frac{\kappa_\nu}{\kappa_\nu + \sigma_\nu}, \quad (57)$$

is very small in the inner layers (e.g., $\epsilon_\nu \approx 2 \times 10^{-3}$ at the midplane). Consequently, J_ν starts to deviate from the thermal source function, which is roughly equal to the Planck function, already in deep layers – see the upper left panel of Fig. 7. One can make these considerations more quantitative by invoking a simple model of radiative transfer in the presence of scattering (see, e.g., Mihalas 1978). In a simple case of depth-independent B_ν and ϵ_ν , the mean intensity is given by

$$J_\nu(\tau_\nu) \approx B_\nu(\tau_\nu) \left[1 + \sqrt{\epsilon_\nu} - \exp(-\sqrt{3\epsilon_\nu} \tau_\nu) \right] / (1 + \sqrt{\epsilon_\nu}). \quad (58)$$

It is clear that $J_\nu \approx B_\nu$ for $\tau_\nu \gtrsim \sqrt{3\epsilon_\nu}$ (called the thermalization depth); while for $\tau_\nu < \sqrt{3\epsilon_\nu}$ the mean intensity J_ν drops below B_ν ; the drop is larger for smaller ϵ_ν . We note that at the surface, $J_\nu(0) \approx \sqrt{\epsilon_\nu} B_\nu$.

The photoionization rate is proportional to an integral of J_ν , while the recombination rate is proportional to an integral of B_ν . As a result, the recombinations dominate over ionizations, which leads to an overpopulation of the hydrogen ground state. For cooler models, the formation of Lyman continuum is different. The electron scattering is not overwhelmingly dominant, so the thermal coupling parameter ϵ is now smaller (ϵ is between 10^{-2} and 10^{-1} in the midplane layers), and the mean intensity decouples from B_ν farther away from the midplane. The Planck function at the frequencies of the Lyman continuum decreases very fast with decreasing temperature, because the Lyman continuum frequencies are in the Wien tail of the Planck function, $B_\nu(T) \propto \exp(-h\nu/kT)$. This decrease in the local value of B_ν is now faster than the decrease

of J_ν which, when going outward, is more and more decoupled from the local temperature. We thus obtain $J_\nu > B_\nu$ throughout most of the atmosphere; consequently the ionizations dominate over recombinations in the Lyman continuum, and hence the hydrogen ground state becomes underpopulated.

Once the Lyman continuum becomes transparent (which happens around $\log m \approx 0$ for all models), b_1 does not change much for NLTE/C models. For NLTE/L models, however, b_1 starts to increase outward above $\log m \approx 0$, which is caused by radiative transfer in $\text{Ly}\alpha$ and other Lyman lines. This is a standard NLTE effect – strong resonance lines cause the lower level to be overpopulated, while the upper level becomes underpopulated with respect to LTE (e.g., Mihalas 1978). This is illustrated in Fig. 4b, which displays the b -factor for the $n = 2$ state of hydrogen. Detailed explanation of the behavior of b_2 is quite analogous to that of b_1 discussed above.

The most interesting quantity predicted by the models is the emergent radiation. Figure 5 compares the emergent flux in the Lyman limit region for the three models, LTE, NLTE/C, and NLTE/L. Only hydrogen and helium lines are taken into account. In the NLTE/C model, the line source functions are computed using NLTE level populations, which in turn were calculated by TLUSDISK by considering the lines to be in detailed radiative balance. Consequently, the predicted line profiles are inconsistent, and we show them only for demonstration purposes. The spectra were computed using program SYNSPEC (Hubeny, Lanz, & Jeffery 1994), which calculates synthetic spectra for model atmospheres or disks previously computed by TLUSTY or TLUSDISK. We assume the turbulent velocity $v_{\text{turb}} = 3880, 770$, and 375 km s^{-1} , for the annuli at $r = 2, 11$, and 20 , respectively. For a clearer display, the final spectra are convolved with a gaussian with $\text{FWHM} = 10 \text{ \AA}$. We stress that the spectra are computed in the rest frame of the annulus; to obtain spectrum received by a distant observer one would have to take into account Doppler velocities, and general relativistic effects (frequency shift, light bending, etc.). As pointed out in the Introduction, we will study here only the rest-frame radiation.

For the hot model, the NLTE/C and NLTE/L models give essentially the same flux across the Lyman discontinuity which in this case virtually disappears. In contrast, the LTE model predicts

the Lyman jump in emission. In the intermediate model, LTE predicts almost non-existent Lyman jump while NLTE/L predicts a weak emission jump. The NLTE/C model predicts a larger emission jump, and spuriously strong emission in the Lyman lines. In the cool model, LTE predicts the Lyman jump in very strong absorption, while the NLTE/L models again predicts essentially smooth spectrum in this region.

The explanation of this behavior follows from the above discussion of the hydrogen departure coefficients b_1 and b_2 (Fig. 4), and from studying the behavior of B_ν , S_ν , J_ν , and ϵ_ν as functions of depth. This is displayed in Fig. 7 for the hot model at $r = 2$, and in Fig. 8 for the cool model at $r = 20$. Let us first consider LTE models. In the hot model, electron scattering completely dominates, so the total opacities at both sides of the Lyman discontinuity are roughly equal; hence both sides of the discontinuity are formed at the same depth. The only difference is the value of the thermal coupling parameter ϵ_ν . Since the thermal opacity on the blue side (ν_b) of the discontinuity is larger than that on the red side (ν_r), we have $\epsilon_{\nu_b} > \epsilon_{\nu_r}$. Consequently, the mean intensity at the red side is more uncoupled from B_ν , and consequently $J_{\nu_b} > J_{\nu_r}$ – see Eq. (58). In fact, this is an interesting manifestation of the classical Schuster mechanism. By the same token, one can understand why the Lyman lines also appear in emission in the hot LTE model.

In the cool model, in contrast, we have a classical LTE jump: the high-opacity (blue) side of the jump is formed much higher than the low-opacity (red) side, because the electron scattering opacity no longer dominates over the thermal opacity. Since the temperature decreases outward, the blue side of the jump is formed at lower temperature, and the flux is consequently lower. In the intermediate model, both effects compete, but the first one wins, so we obtain a weak emission jump.

NLTE effects modify this picture significantly. In the hot model, the red side of the Lyman jump remains almost unchanged by NLTE effects because the departure coefficient b_2 is close to unity around the thermalization depth of the Balmer continuum. In the Lyman continuum, the thermal coupling parameter $\epsilon_{\nu_b} > \epsilon_{\nu_r}$ as discussed above. However, in NLTE one has to modify

Eq. (58) to read

$$J_\nu(\tau_\nu) \approx S_\nu^{\text{th}}(\tau_\nu) \left[1 + \sqrt{\epsilon_\nu} - \exp(-\sqrt{3\epsilon_\nu} \tau_\nu) \right] / (1 + \sqrt{\epsilon_\nu}), \quad (59)$$

where S_ν^{th} is the thermal source function. In the case of Lyman continuum, it is roughly given by $S_\nu^{\text{th}} \approx B_\nu/b_1$. Since $b_1 > 1$ in the continuum-forming layers (see Fig. 4a), we have $S_\nu^{\text{th}} < B_\nu$. We see that the effect of an increased thermal coupling parameter ϵ_ν at the Lyman continuum frequencies (which tends to increase the emergent intensity) is offset by a decrease of the thermal source function. The latter results from a predominance of recombinations over ionizations, as explained above.

Finally, we explain why we obtain a somewhat higher flux in the Lyman continuum for the NLTE/C models than for NLTE/L models. This is given by the fact that $b_1(\text{NLTE/C}) < b_1(\text{NLTE/L})$ all the way from the surface to deep layers (see Fig. 4a), which in turn is the effect of $\text{Ly}\alpha$ and other Lyman lines. Because of low density, the photon destruction parameter ϵ is rather small and therefore the thermalization depth is rather large – much larger than the depth of formation (see, e.g., Mihalas 1978). Consequently, the thermal source function in the Lyman continuum, $S_\nu^{\text{th}} \approx B_\nu/b_1$, is smaller in the NLTE/L model, and consequently the emergent flux is lower.

Figure 6 displays the EUV continuum. As we have discussed in Paper I, NLTE models produce the He II Lyman jump in emission for the hot annuli. For cooler annuli, both LTE and NLTE models produce a strong absorption in the He II Lyman jump. Both NLTE/C and NLTE/L models produce very similar results.

Having computed models of vertical structure, we can verify that neglecting Compton scattering was indeed a legitimate approximation. To this end, we compute the appropriate Compton y parameter which specifies whether a photon will be significantly influenced by comptonization in traversing the medium. For non-relativistic electrons, the Compton y parameter is given by (Rybicki & Lightman 1979)

$$y = \frac{4kT}{m_e c^2} \max(\tau_{\text{es}}, \tau_{\text{es}}^2) \quad (60)$$

where τ_{es} is the total electron-scattering optical depth of the medium. In the case in which thermal absorption is not negligible, the τ_{es} depends on frequency, and is defined by (Rybicki & Lightman 1979, their eq. 7.42)

$$\tau_{\text{es}}(\nu) \approx \left(\frac{\sigma_\nu / \kappa_\nu}{1 + \kappa_\nu / \sigma_\nu} \right)^{1/2} = (1 - \epsilon_\nu) \epsilon_\nu^{-1/2}, \quad (61)$$

where the second equality follows from Eq. (57). Strictly speaking, the above formulae are derived for a homogeneous medium. We may nevertheless use them for some characteristic (averaged) values of structural parameters. The Compton scattering would be most important in the hottest model. Taking $T = T_{\text{eff}}$ and the characteristic ϵ for the Lyman continuum frequencies equal to 10^{-2} (see Fig.7), we obtain for $y \approx 5 \times 10^{-3}$. Even the upper limit for y , taking the midplane values of $T \approx 3 \times 10^5$ and $\epsilon \approx 2 \times 10^{-3}$ (which would give a largely overestimated value of y because the local temperature is lower and the parameter ϵ is higher) yields $y \approx 10^{-1}$, which is still well below unity. Therefore Compton scattering is never very important for the models considered here.

In conclusion, there are several NLTE effects; for hot and cool models they decrease the magnitude of the Lyman discontinuity as compared to LTE models, or to simplified NLTE/C models, while for the intermediate temperatures they somewhat increase the Lyman jump. We also find that for hot annuli, the NLTE/C models are sufficient for predicting the emergent *continuum* radiation, while for cooler annuli the NLTE/C models produce a somewhat higher flux in the Lyman continuum, and spuriously strong emissions in the Lyman lines.

We stress again that the present paper is devoted to studying a few representative annuli of an AGN accretion disk model. We do not aim here to answer the important question of whether the present models will alleviate the long-standing Lyman jump problem, namely that the theoretical models predict a significant jump, while the observed jump is virtually non-existent. The problem arose from early calculations by Kolykhalov & Sunyaev (1984); a comprehensive review of the current status was presented by Blaes (1998). To address this problem, we have to compute theoretical models and emergent spectra for all annuli of a disk and integrate them using the appropriate general relativistic transfer function (Cunningham 1975; Agol 1997). Also, we should

take into account effects of metal lines, which was recently found to be quite important (Hubeny & Hubeny 1998; Agol, Blaes, & Hubeny 1998). We shall defer this study to a future paper of this series.

3.2. Effects of Viscosity

The most important parameter influencing the model structure is α_0 . We first study the effects of changing α_0 , while keeping the remaining viscosity parameters fixed. We take $\zeta_0 = 0$ (i.e., a constant viscosity in the inner region); $m_d = 10^{-2}$ (i.e., the viscosity starts to decrease with m only for $m/m_0 = 10^{-2}$; in other words, 99% of the mass of the disk column has a constant viscosity); and $\zeta_1 = 2/3$. Since the total column mass, m_0 , is proportional to $1/\alpha_0$ – see Eq. (18), we may think of effects of changing the value of the parameter α_0 being in fact effects of changing the disk column mass. We stress again that our study concerns the behavior of the individual disk annuli and its sensitivity to the adopted value of α_0 . In reality, it is not clear whether the same value of α_0 should be considered for all annuli of a given disk or not. This will only be solved by future detailed MHD simulations similar to those of Stone et al. (1996).

Figure 9 shows the results for the hot annulus; the upper panel displays the temperature, the middle panel the density, and the lower panel the emergent flux, for the NLTE/C models for $\alpha_0 = 0.3, 0.1, 0.03, 0.01$, and 0.005 . The behavior of density is easy to understand. The total column mass, m_0 , is directly proportional to $1/\alpha_0$ – see Eq. (18). The total disk height does not depend on viscosity for radiation-pressure-dominated disks (see Eq. 53); therefore the density in the inner regions is proportional to m_0 – see Eq. (55) – and consequently $\rho(m \approx m_0) \propto 1/\alpha_0$. This is demonstrated on the middle panel of Fig. 9. Consequently, the thermal coupling parameter ϵ (which is proportional to density), is larger for smaller α_0 .

The behavior of temperature is more complicated, since it follows from several competing mechanisms. First, we write a simple analytic formula derived by Hubeny (1990a) which gives a

reasonably accurate estimate of the local temperature, viz.,

$$T^4(\tau) = \frac{3}{4} T_{\text{eff}}^4 \left[\tau \left(1 - \frac{\tau}{2\tau_{\text{tot}}} \right) + \frac{1}{\sqrt{3}} + \frac{1}{3m_0 \kappa_B(\tau)} \frac{w(m)}{\bar{w}} \right], \quad (62)$$

where τ is the flux-mean optical depth, $d\tau = \chi_H dz = (\chi_H/\rho) dm$; τ_{tot} is the flux-mean optical thickness at the midplane; and $\kappa_B(\tau)$ is the Planck-mean opacity, defined by

$$\kappa_B = \int_0^\infty (\kappa_\nu/\rho) B_\nu d\nu / B, \quad (63)$$

where B is the frequency-integrated Planck function, $B(T) = \int_0^\infty B_\nu(T) d\nu = (\sigma/\pi)T^4$. This formula is easy to understand. The term $\tau + 1/\sqrt{3}$ in the square bracket is the same as for the classical LTE-grey semi-infinite model stellar atmospheres in radiative equilibrium (i.e., no energy generated in the atmosphere). The “correction” $(1 - \tau/2\tau_{\text{tot}})$ reflects the fact that the disk has a finite total optical thickness; while the third term describes the energy generation in the disk due to viscous dissipation. Notice also that the Planck-mean opacity contains the thermal absorption coefficient, κ_ν , while the flux-mean opacity contains the total absorption coefficient, χ_ν . The fact that the dissipation term of Eq. (62) contains the Planck mean opacity is easy to understand, since it is the thermal absorption, not scattering, that contributes to the global energy balance. In the case of dominant electron scattering, the relation between the flux-mean optical depth, τ , and the column mass, m , is particularly simple, $\tau \approx 0.34m$ (if helium is doubly ionized), or $\tau \approx 0.31m$ (if helium is singly ionized), as discussed in Sect. 3.1.

As follows from Eq. (62), the temperature at the midplane is roughly given by

$$T^4(\tau_{\text{tot}}) = \frac{3}{4} T_{\text{eff}}^4 \left[\frac{\tau_{\text{tot}}}{2} + \frac{1}{3m_0 \kappa_B(\tau_{\text{tot}})} \right], \quad (64)$$

where we assume that the disk is optically thick, $\tau_{\text{tot}} \gg 1$, and the local viscosity at the midplane roughly equal to the averaged viscosity. Quantity $m_0 \kappa_B(\tau_{\text{tot}})$ is very roughly equal to the total Planck-mean optical depth of the disk. We write $m_0 \kappa_B(\tau_{\text{tot}}) = \bar{\epsilon} \tau_{\text{tot}}$. Since $\bar{\epsilon}$ is proportional to κ_B/χ_H , it may be called the “averaged thermal coupling parameter”. The midplane temperature then becomes

$$T^4(\tau_{\text{tot}}) = \frac{3}{4} T_{\text{eff}}^4 \left(\frac{\tau_{\text{tot}}}{2} + \frac{1}{3\bar{\epsilon} \tau_{\text{tot}}} \right), \quad (65)$$

If the electron scattering is negligible, $\bar{\epsilon} \approx 1$, and the second term in Eq. (65) is negligible compared to the first one in the case of optically thick disks. In fact, the disk behaves like a normal stellar atmosphere. However, as soon as the averaged thermal coupling parameter becomes small, the second term in Eq. (65) starts to contribute. This is indeed illustrated in the upper panel of Fig. 9. For the lowest α_0 , $\alpha_0 = 0.005$, the total optical depth is very large, and consequently the central temperature is high. Increasing α_0 , the total optical depth decreases, and so does the central temperature. However, with increasing α_0 the density decreases, and therefore the thermal coupling parameter $\bar{\epsilon}$ also decreases. Hence the second (viscous-heating) term of Eq. (65) starts to make appreciable contribution to the central temperature, which first levels off and then starts to increase even if the total optical depth decreases (see the last curve for $\alpha_0 = 0.3$). Since the second term of Eq. (65) makes roughly the same contribution at all depths, we see a similar increase of local temperature at all depths.

At the top of the disk, density decreases exponentially, and consequently $\bar{\epsilon}$ decreases faster than $w(m)/\bar{w}$, which is assumed to be a simple power law (recall that $w(m)/\bar{w} \propto (m/m_0)^{2/3}$ for the models displayed in Fig. 9). Since for the model with the largest α_0 , $\alpha_0 = 0.3$, the averaged thermal coupling parameters is so small that the second term in fact determines the temperature structure. Consequently, the surface temperature begins to increase to large values (this effect is better seen in Fig. 12 where we consider a lower ζ_1 and therefore a higher viscosity in the upper layers). However, as discussed by Hubeny (1990a), this increase is partly spurious, because in computing the Planck-mean opacity we have included only lines (and continua) of hydrogen and helium. In reality, however, there is a host of other lines of light elements which operate in the upper layers (e.g., the resonance lines of C IV, N V, O VI, and higher ions of S, Ne, Fe, etc., for even higher temperatures). Including these lines will increase the Planck-mean opacity significantly, which physically means that we are including efficient mechanisms which are able to radiate the dissipated energy away.

The lower panel of Fig. 9 shows the continuum flux for all models. The Lyman jump varies from being almost non-existent for the low- α_0 models, to a weak absorption jump for the high- α_0

models. As explained above, the appearance of the Lyman jump is a result of a competition of two mechanisms: the overpopulation of the ground state of hydrogen, which decreases the source function and therefore the emergent flux in the Lyman continuum; and a higher thermal coupling parameter which causes the mean intensity in the Lyman continuum frequencies to be more coupled to the thermal source function, and therefore causes the emergent flux to be higher. In the present case, going to higher α_0 decreases density in the inner layers, therefore causing the hydrogen ground state to be more and more overpopulated, and since this is a dominant effect, the flux in the Lyman continuum decreases with increasing α_0 , so the Lyman jump is driven to a somewhat stronger absorption.

In contrast, the magnitude of the He II Lyman jump decreases with increasing α_0 , from being a very conspicuous emission jump at $\alpha_0 \lesssim 0.03$ to a modest emission jump at $\alpha_0 = 0.3$. This is explained by the fact that the strong jump at $\alpha_0 \lesssim 0.03$ is essentially caused by the Schuster mechanism discussed above. When going to higher α_0 the density decreases, and the electron scattering is more and more important; the jump thus becomes weaker. However, it is important to realize that the number of He II ionizing photons remains roughly the same for all models, since the flux at high frequencies ($\nu \gtrsim 1.7 \times 10^{16}$ Hz) is higher for higher α_0 ; this is a consequence of higher temperature in the continuum-forming region – see the upper panel of Fig. 9.

Figure 10 presents an analogous comparison of models with various values of α_0 for a “cool” annulus, $T_{\text{eff}} = 18,000$ K. The behavior of models is similar to that of the hot annulus, although the effects of viscosity are generally weaker. The total column mass and the inner density are proportional to $1/\alpha_0$, as in the previous case. The central temperature now decreases monotonically with increasing α_0 because the electron scattering is not dominant and therefore the second term in Eq. (65) is not very important. The Lyman jump varies from a weak emission for high- α_0 models to a weak absorption for low- α_0 models. This follows from the fact that for increasing α_0 the density decreases, so the magnitude of NLTE effects increases. In the present case, the ground state of hydrogen becomes more underpopulated, and consequently the flux in the Lyman continuum increases.

Next, we examine the effects of changing the other viscosity parameters. In Fig. 11, we display the models of the hot annulus computed for fixed α_0 ($\alpha_0 = 0.1$) and the power law exponents ($\zeta_0 = 0$ and $\zeta_1 = 2/3$), and for several values of the division mass, m_d . The division mass is varied from $m_d = 1$ (i.e., no inner region of constant viscosity), to $m_d = 0.3, 0.1, 0.03$, and 0.01 . As expected, the only interesting effect is the behavior of density in the inner layers, which is governed by Eq. (55). The central temperature is the largest for $m_d = 1$ because the central density, and thus the thermal coupling parameter, are lowest. The emergent flux is only weakly influenced by changing m_d ; a modest change of the flux is seen in the hydrogen and He II Lyman continuum which are the most sensitive to the thermal coupling parameter.

Finally, Fig. 12 displays the effect of changing ζ_1 , $\zeta_1 = 1, 2/3, 1/2$, and $1/3$, for $\alpha_0 = 0.1$, $m_d = 1$, for the hot annulus ($r = 2$). For $\zeta_1 \gtrsim 1/2$, the only appreciable effects are seen in the behavior of density in inner layers. The overall behavior of the models is easily explained by the same considerations as above. For the model with the lowest ζ_1 , $\zeta_1 = 1/3$, the local viscosity in the upper layers is so high that we see the effects of temperature runaway at $m \approx 5 \times 10^{-3}$. Decreasing the value of ζ_1 still would increase this instability. However, as discussed above, we cannot study this effect with simple H-He models, and we leave this problem to a future paper.

3.3. Comparison with the Local α -viscosity Approach

As discussed in Sect. 2.2, we consider the depth-dependent kinematic viscosity as a step-wise power law function given by Eqs. (22) – (25). In contrast, the local α -prescriptions, e.g., the variant suggested by Dörrer et al. (1996), considers the kinematic viscosity in the form given by Eqs. (13), with the turbulent velocity given by

$$v_{\text{turb}} = c_s \frac{\tau + \sqrt{P_{\text{gas}}/P}}{\tau + 1}, \quad (66)$$

This approach essentially considers the viscosity being proportional to the gas pressure at low optical depths, while being proportional to the radiation pressure at large depths; τ is the Rosseland mean optical depth.

We can compute an “effective α -parameter” in such a way that the two prescriptions give the same value of local viscosity,

$$\alpha_{\text{eff}}(m) = \frac{w(m)}{h v_{\text{turb}}(m)}. \quad (67)$$

Since our parameterization does not take viscosity to be proportional to the local turbulent velocity, the resulting α_{eff} will be depth-dependent.

In Fig. 13, we plot α_{eff} for the hot annulus ($r = 2$), and for various viscosity parameters. We see that the values of α_{eff} for our standard model, $\alpha_0 = 0.1$, $\zeta_0 = 0$, $\zeta_1 = 2/3$, and $m_{\text{d}}/m_0 = 0.01$ are located in a reasonable range of $0.02 \lesssim \alpha_{\text{eff}} \lesssim 0.5$. The behavior of α_{eff} as a function of depth is easily understood. In the inner layers, $v_{\text{turb}} = (P/\rho)^{1/2} \approx (P_{\text{rad}}/\rho)^{1/2}$. Since the optical depth is large, the radiation pressure can be approximated by the thermodynamic equilibrium form, $P_{\text{rad}} \propto T^4$. In the model with $m_{\text{d}}/m_0 = 0.01$ density is roughly constant for $m_{\text{d}} \lesssim m \leq m_0$. Consequently, $v_{\text{turb}} \propto T^2$. To first order, $T^4 \propto \tau \propto m$ (see Eq. 62), so that finally $v_{\text{turb}} \propto m^{1/2}$, and $\alpha_{\text{eff}} \propto m^{-1/2}$ for $m > m_{\text{d}}$. This is indeed seen in the upper and lower panels of Fig. 13; α_{eff} decreases with m somewhat slower than $m^{-1/2}$ because the temperature increases slower than $T^4 \propto m$ – in fact, $T^4 \propto (m - m^2/2m_0)$.

For models with a single power law viscosity (i.e., $m_{\text{d}} = m_0$), the behavior of α_{eff} in the inner layers can also be easily understood. Here $w(m) \propto m^\zeta$ (we write ζ instead of ζ_1 to simplify the notation), so the density varies as $\rho(m) \propto 1/w(m) \propto m^{-\zeta}$. The radiation pressure scales, as discussed above, as $P_{\text{rad}} \propto m$. Consequently, $v_{\text{turb}} \propto m^{(\zeta+1)/2}$, and thus $\alpha_{\text{eff}} \propto m^{(\zeta-1)/2}$. This is demonstrated in the middle panel of Fig. 13; for instance, we see that for $\zeta = 1$, α_{eff} is indeed almost constant in the inner layers. In the outer layers, the density decreases outward faster than $w(m)$, so α_{eff} decreases faster than $m^{(\zeta-1)/2}$.

In the gas-pressure-dominated regions, $v_{\text{turb}} = (P_{\text{gas}}/\rho)^{1/2}$, so we have $v_{\text{turb}} \propto T$, and thus $\alpha_{\text{eff}} \propto w(m)/T(m)$. In the outer layers, the temperature is roughly constant with m , so that $\alpha_{\text{eff}} \propto w(m) \propto m^{\zeta_1}$. Again, this is clearly seen in Fig. 13.

The important point to realize is that although the local value of α_{eff} varies significantly, its

influence on the disk structure is rather small. Consider for instance the middle panel of Fig. 13, and compare it to Fig. 12, which displays the same models. Although α_{eff} differs by several orders of magnitude, the disk structure is hardly affected. From the point of view of constructing detailed models of vertical structure of AGN disks this is a good news, because the most uncertain part of physics – the viscous dissipation – has relatively small effect on the computed structure. However, we should bear in mind that this study was limited to considering a “well-behaved” viscosity which smoothly decreases towards the disk surface. When one assumes, for instance, that the viscous dissipation is concentrated mostly in the outer layers (e.g., Sincell & Krolik 1997), the overall vertical structure may be significantly different. We plan to study such non-standard models in future papers of this series.

4. CONCLUSIONS

We have calculated several representative models of vertical structure of an accretion disk around a supermassive Kerr black hole. The interaction of radiation and matter is treated self-consistently, taking into account departures from LTE for calculating both the disk structure and the radiation field. The viscosity is parameterized through the parameter α_0 that describes the vertically averaged viscous stress, and two power-law exponents ζ_0 and ζ_1 , and the division point m_d between these two forms. The disk structure and emergent radiation is sensitive mainly to the values of α_0 , while the other parameters influence the disk structure to a much lesser extent. However, although the detailed shape of the predicted spectrum is sensitive to adopted α_0 , the overall appearance of the spectrum is quite similar in all cases.

We have shown that effects of departures from LTE are very important for determining the disk structure and emergent radiation, particularly for hot and electron-scattering dominated disks. We have shown that at least for the disk parameters studied in this paper, NLTE effects typically tend to diminish the value of the Lyman jump; in hot models they suppress the Schuster mechanism by which the LTE models produce a strong emission jump, and in cooler models they increase the flux in the Lyman continuum due to an underpopulation of the hydrogen ground

state. Also, we have shown that relaxing the approximation of detailed radiative balance in the hydrogen and helium lines (i.e., computing the so-called NLTE/L models) changes the predicted line profiles significantly, but otherwise does not yield significant changes in computed vertical structure or emergent continuum flux. This result shows that for estimating the *continuum* radiation of AGN disks composed of hydrogen and helium, the NLTE/C models provide a satisfactory approximation.

So far, we have limited our analysis to a simple H-He chemical composition. A preliminary study (Hubeny & Hubeny 1998) indicates that the effects of numerous metal lines on the predicted spectral energy distribution of AGN disks may be quite significant. However, that study used a simplified approach in which the vertical structure was fixed by a H-He model, while the line opacity was taken into account only in the spectrum synthesis, assuming LTE source function in metal lines. Such an approach is inconsistent, since, first, the metal lines may change the disk vertical structure (the so-called metal line blanketing effects, long known from the theory of classical stellar atmospheres) and, second, the source function in metal lines may depart significantly from the LTE value. We will therefore need to construct self-consistent, fully metal-line-blanketed models of vertical structure of AGN disks, taking into account effects of literally millions of spectral lines in NLTE. A work of this project is under way, and will be reported in a future paper of this series.

The results presented here do not indicate any fatal flaw of the AGN accretion disk paradigm. In contrast, they show that one of the previous critical arguments against the accretion disk paradigm, the magnitude of the Lyman jump, essentially disappears when increasing a degree of realism of the modeling procedure by relaxing previous simplifying approximations, in particular the local thermodynamic equilibrium and a simplified vertical disk structure. However, this study has concentrated on only one aspect of the problem, the spectral energy distribution in the optical, UV, and EUV region. Many questions, such as the overall spectral energy distribution of the whole disk, the effects of external irradiation, the continuum polarization, etc., remain to be explored in detail. This is exactly what we intend to do in future papers of this series.

This work was supported in part by NASA grant NAGW-3834 and by the HST/STIS project funds. We thank Eric Agol, Omer Blaes, and Julian Krolik for valuable discussions and very helpful comments on the manuscript.

REFERENCES

Abramowicz, M.A., Lanza, A., & Percival, M.J. 1997, *ApJ*, 479, 179

Agol, E. 1997, PhD Thesis, University of California, Santa Barbara

Agol, E., Hubeny, I., & Blaes, O. 1998, in *Accretion Processes in Astrophysical Systems: Some Like it Hot*, ed. by S.S. Holt & T. Kallman (in press)

Alloin, D., Pelat, D., Phillips, M., & Whittle, M. 1985, *ApJ*, 288, 205

Antonucci, R.R.J. 1992, in *Testing the AGN Paradigm*, ed. by S.S. Holt, S.G. Neff, & C.M. Urry, 486

Antonucci, R.R.J., Kinney, A.L., & Ford, H.C. 1989, *ApJ*, 342, 64

Balbus, S.A., & Hawley, J.F. 1991, *ApJ*, 376, 214

Blaes, O. 1998, in *Accretion Processes in Astrophysical Systems: Some Like it Hot*, ed. by S.S. Holt & T. Kallman (in press)

Blaes, O., & Agol, E. 1996, *ApJ*, 469, L41

Coleman, H.H. 1994, PhD thesis, Univ. of Texas

Cunningham, C. 1975, *ApJ*, 202, 788

Dörrer, T., Riffert, H., Staubert, R., & Ruder, H. 1996, *A&A*, 311, 69

Eardley, D.M., & Lightman, A.P. 1975, *ApJ*, 200, 187

Hubeny, I. 1988, *Comp. Phys. Commun.* 52, 103

Hubeny, I. 1990a, *ApJ*, 351, 632

Hubeny, I. 1990b, in *IAU Colloquium 129, Structure and Emission Properties of Accretion Disks*, ed. by C. Bertout et al. (Gif sur Yvette: Editions Frontières), p. 227

Hubeny, I. 1992, in *The Atmospheres of Early-Type Stars*, ed. by U. Heber and C.J. Jeffery, *Lecture Notes in Phys.* 401, (Berlin: Springer), 377

Hubeny, I., Hummer, D.G., & Lanz, T. 1994, *A&A*, 282, 157

Hubeny, I., & Lanz, T. 1995, ApJ, 439, 875

Hubeny, I., Lanz, T., & Jeffery, C. S. 1994, in “Newsletter on Analysis of Astronomical Spectra” No. 20, ed. C. S. Jeffery (St Andrews Univ.), 30

Hubeny, I., & Hubeny, V. 1997, ApJ, 484, L37 (Paper I)

Hubeny, I., & Hubeny, V. 1998, in Accretion Processes in Astrophysical Systems: Some Like it Hot, ed. by S.S. Holt & T. Kallman, (in press)

Kolykhalov, P.I., & Sunyaev, R. A. 1984, Adv. Sp. Res. 3, 249

Koratkar, A. 1998, in Accretion Processes in Astrophysical Systems: Some Like it Hot, ed. by S.S. Holt & T. Kallman (in press)

Kříž, S., & Hubeny, I. 1986, Bull. Astron. Inst. Czechosl., 37, 129

Laor, A. 1990, MNRAS, 246, 369

Laor, A., & Netzer, H. 1989, MNRAS, 238, 897

Lynden-Bell, D., & Pringle, J. E. 1974, MNRAS, 168, 603

Malkan, M. A. 1983, ApJ, 268, 582.

Malkan, M. A., & Sargent, W.L.W. 1982, ApJ, 254, 22

Mihalas, D. 1978, Stellar Atmospheres (San Francisco: Freeman)

Novikov, I.D., & Thorne, K.S. 1973, in Black Hole Astrophysics, ed. by De Witt, C., & De Witt, B. (Gordon and Breach, New York), p. 343

Page, D.N., & Thorne, K.S. 1974, ApJ, 191, 499

Riffert, H., & Harold, H. 1995, ApJ, 450, 508

Ross, R.R., Fabian, A.C., & Mineshige, S. 1992, MNRAS, 258, 189

Rybicki, G.B., & Lightman, A.P. 1979, Radiative Processes in Astrophysics, (New York: Wiley)

Shakura, N. I., & Sunyaev, R. A. 1973, A&A, 24, 337

Shaviv, G., & Wehrse, R. 1986, A&A, 259, L5

Shields, G. 1978, *Nature* 272, 706

Shields, G.A., & Coleman, H.H. 1994, in *Theory of Accretion Disks - 2*, ed. by W.J. Duschl et al. (Dordrecht: Kluwer), 223.

Shu, F.H. 1991, *The Physics of Astrophysics I. Radiation*, (Mill Valley: University Science Books)

Sinell, M.W., & Krolik, J.H. 1997, *ApJ*, 476, 605

Speith, R., Riffert, H., & Ruder, H. 1995, *Comp. Phys. Commun.* 88, 109

Stone, J.M., Hawley, J.F., Balbus, S.A., & Gammie, C.F. 1996, *ApJ*, 463, 656

Störzer, H., & Hauschildt, P.H. 1994, *A&A*, 289, 45

Störzer, H., & Hauschildt, P.H., & Allard, F. 1994, *ApJ*, 437, L91

Sun, W.-H., & Malkan, M.A. 1989, *ApJ*, 346, 68.

Wehrse, R., Störzer, H., & Shaviv, G. 1993, *Ap&SS* 205, 163

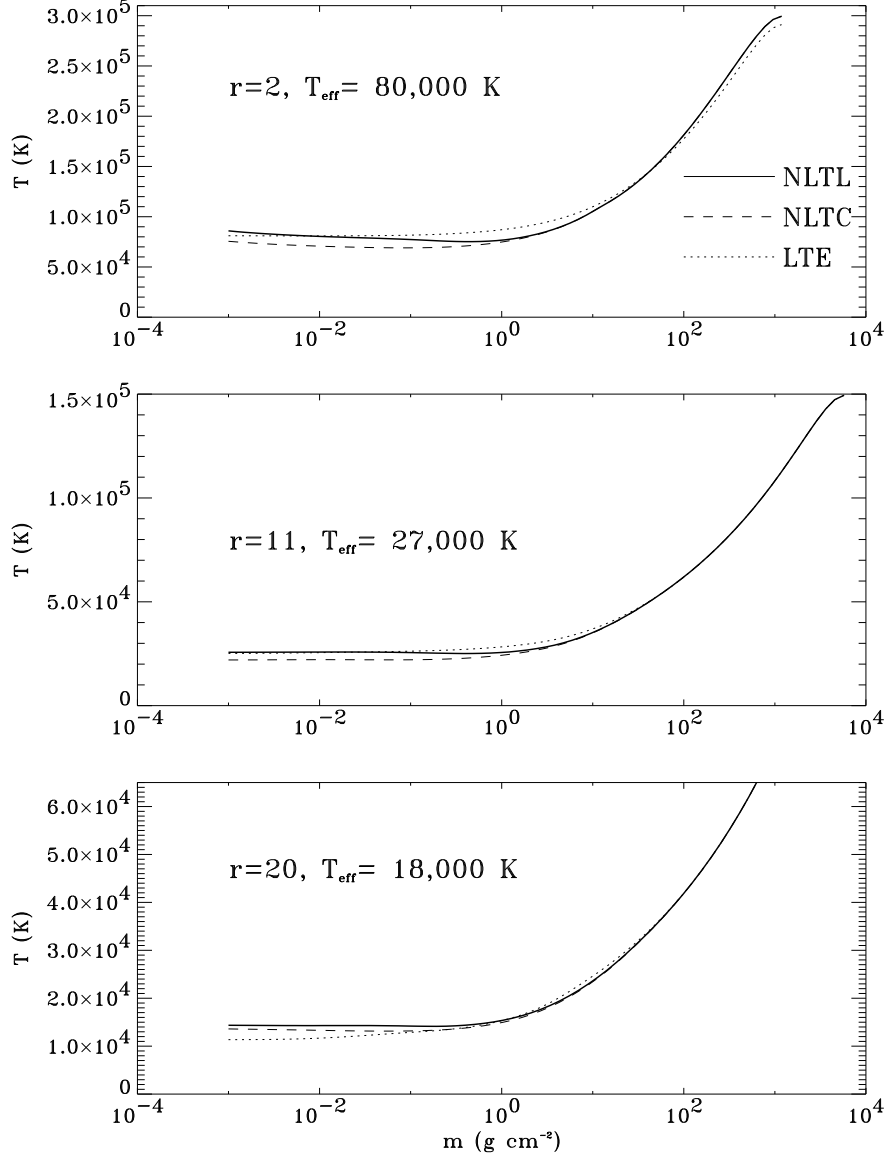


Fig. 1.— Temperature as a function of depth for three annuli at $r = 2$ – upper panel; $r = 11$ – middle panel; and $r = 20$ – lower panel; for a disk model with the mass of the black hole, $M = 2 \times 10^9 M_\odot$, the mass accretion rate $\dot{M} = 1 M_\odot/\text{yr}$, and the maximum stable rotation, $a/M = 0.998$. The viscosity parameters are taken $\alpha_0 = 0.1$, $\zeta_0 = 1$, $\zeta_1 = 2/3$, and $m_d = 0.01$. For all annuli, the thick line is the NLTE/L model, the dashed line the NLTE/C (i.e., NLTE with continua only) model, and the dotted line is the LTE model.

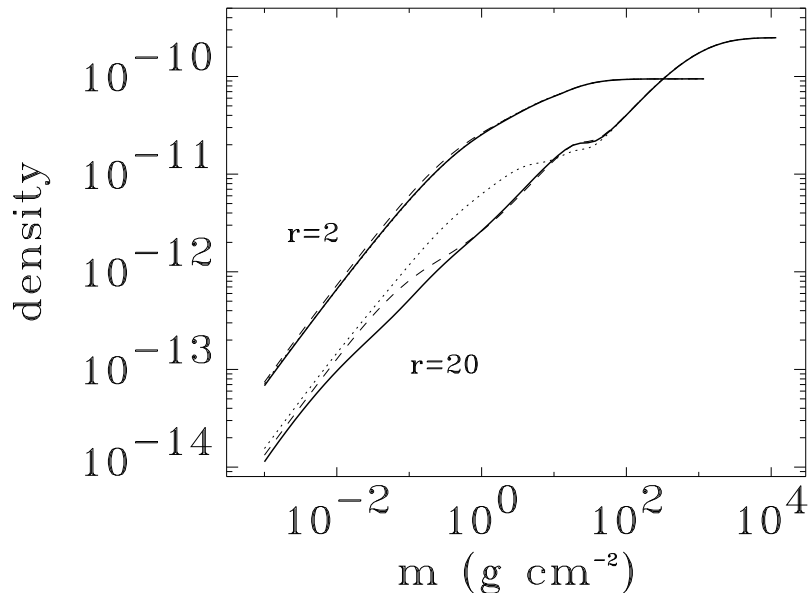


Fig. 2.— Mass density (in g cm^{-3}) for the model annulus at $r = 2$ – the upper curves, and for $r = 20$ – the lower curves; for the same models as displayed in Fig. 1. We did not show the $r = 11$ model because its behavior is quite analogous to that of the $r = 20$ model.

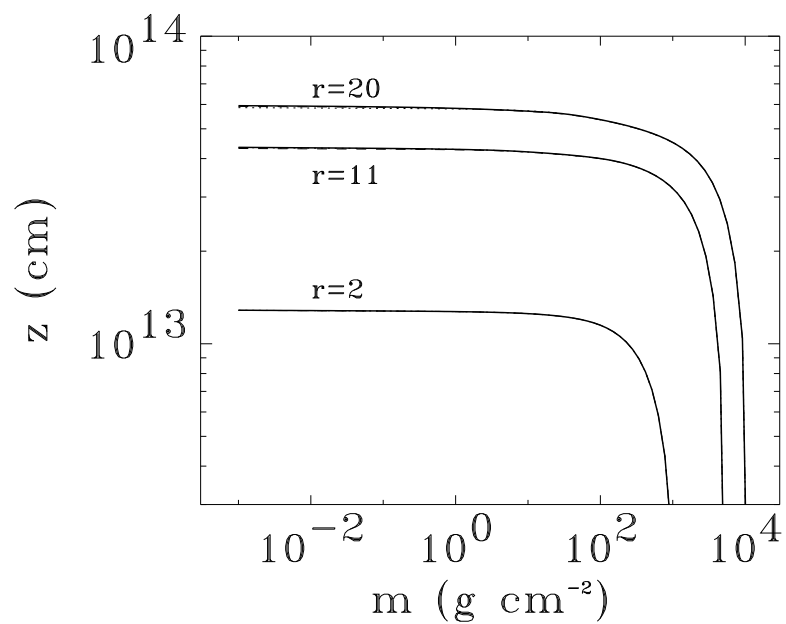


Fig. 3.— Vertical distance from the disk plane as a function of column mass for the model disk annulus at $r = 2$ (lower curves); $r = 11$ (middle curves); and $r = 20$ (upper curves), for the same models as displayed in Fig. 1. Notice that NLTE effects upon the z vs. m relation are quite small.

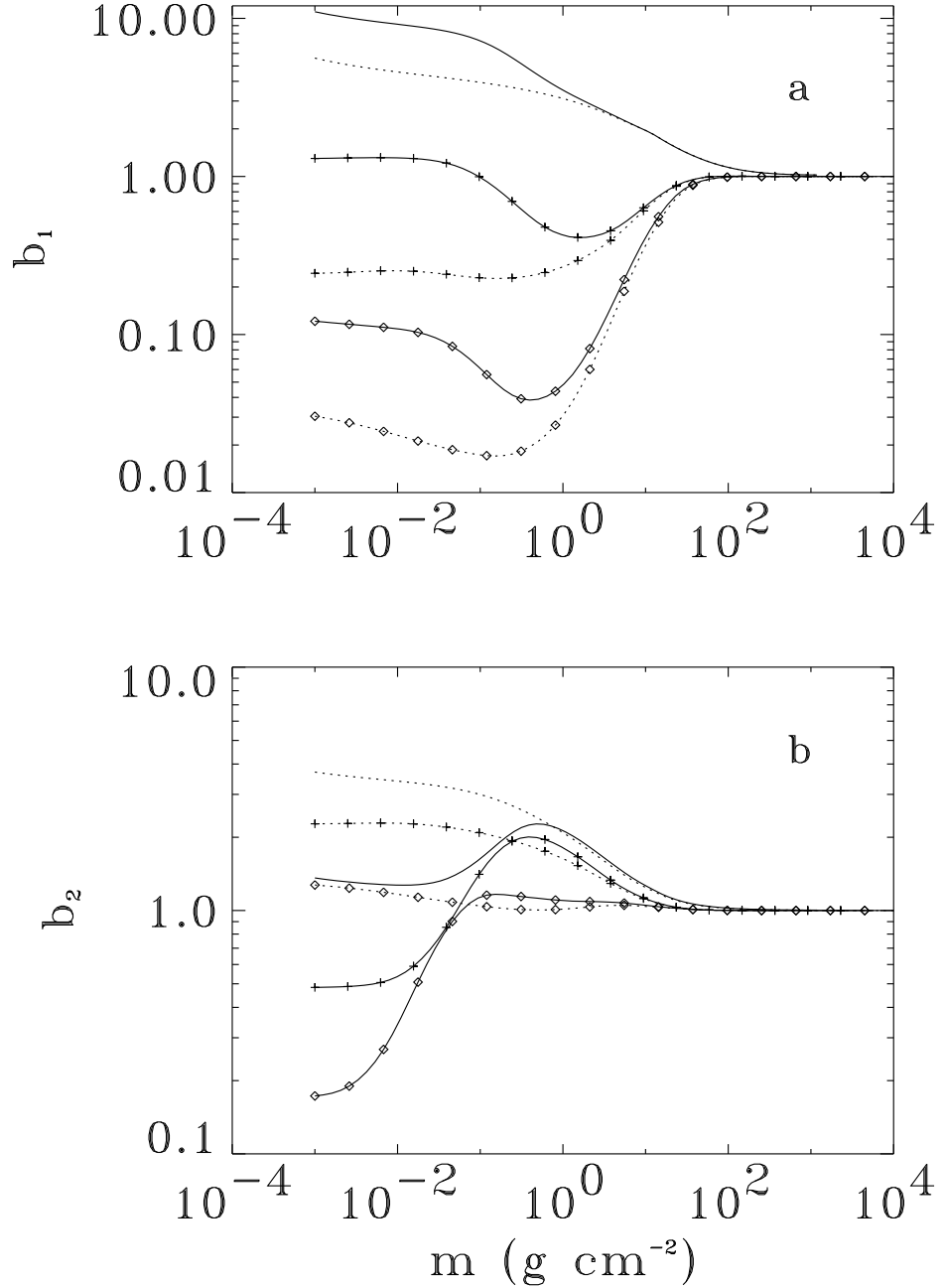


Fig. 4.— NLTE departure coefficients for the hydrogen ground level (a), and the $n = 2$ level (b); for the NLTE/C models (dotted lines), and NLTE/L models (full lines). The lines without additional symbols correspond to the model annulus at $r = 2$; the lines with additional “+” signs to the $r = 11$ models, and with diamonds to $r = 20$ models.

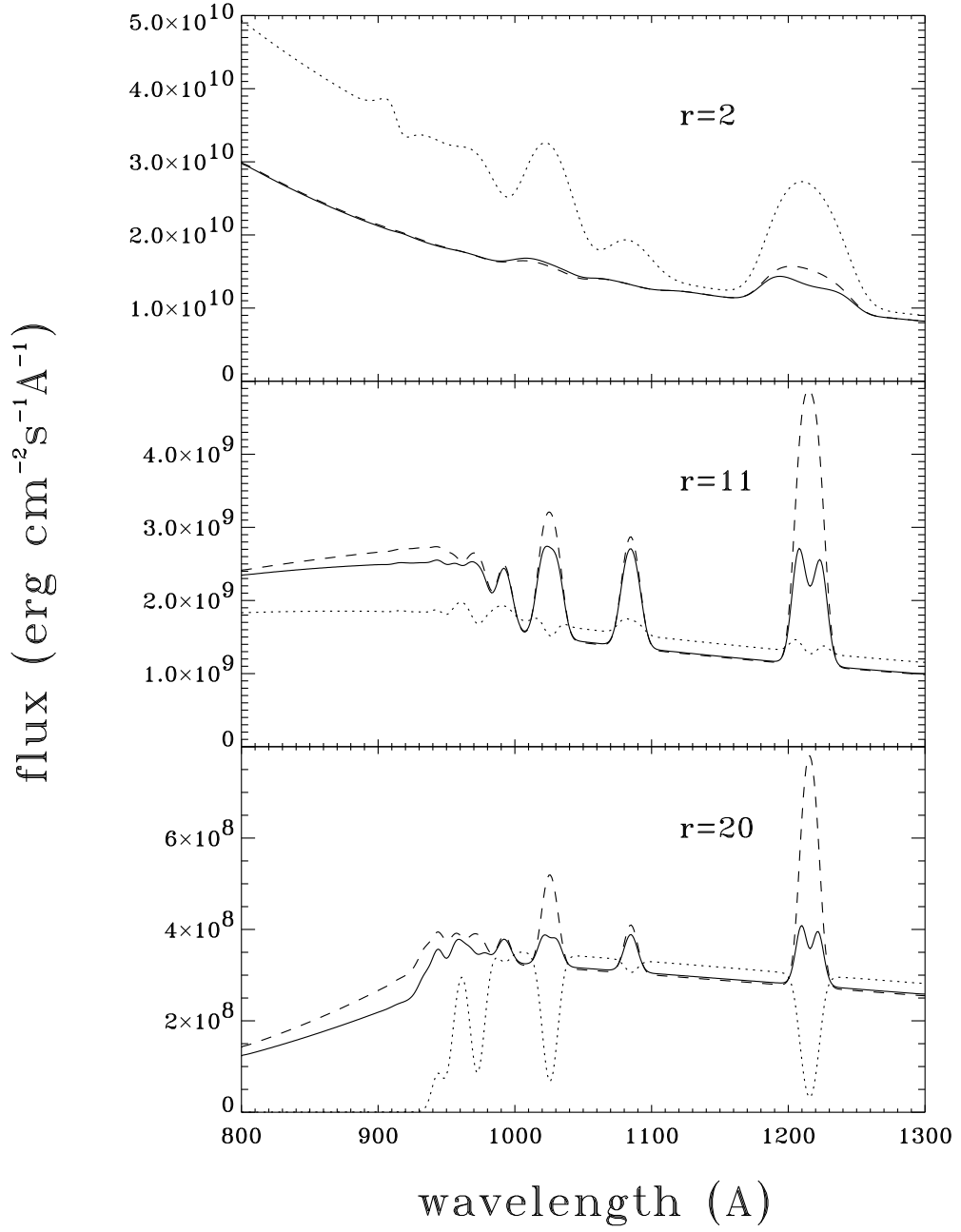


Fig. 5.— A comparison of emergent flux in the region around the Lyman discontinuity for the NLTE/L model (full line); NLTE/C model (dashed line), and LTE model (dotted line) of the model disk annulus at $r = 2$ (upper panel), $r = 11$ (middle panel), and $r = 20$ (lower panel).

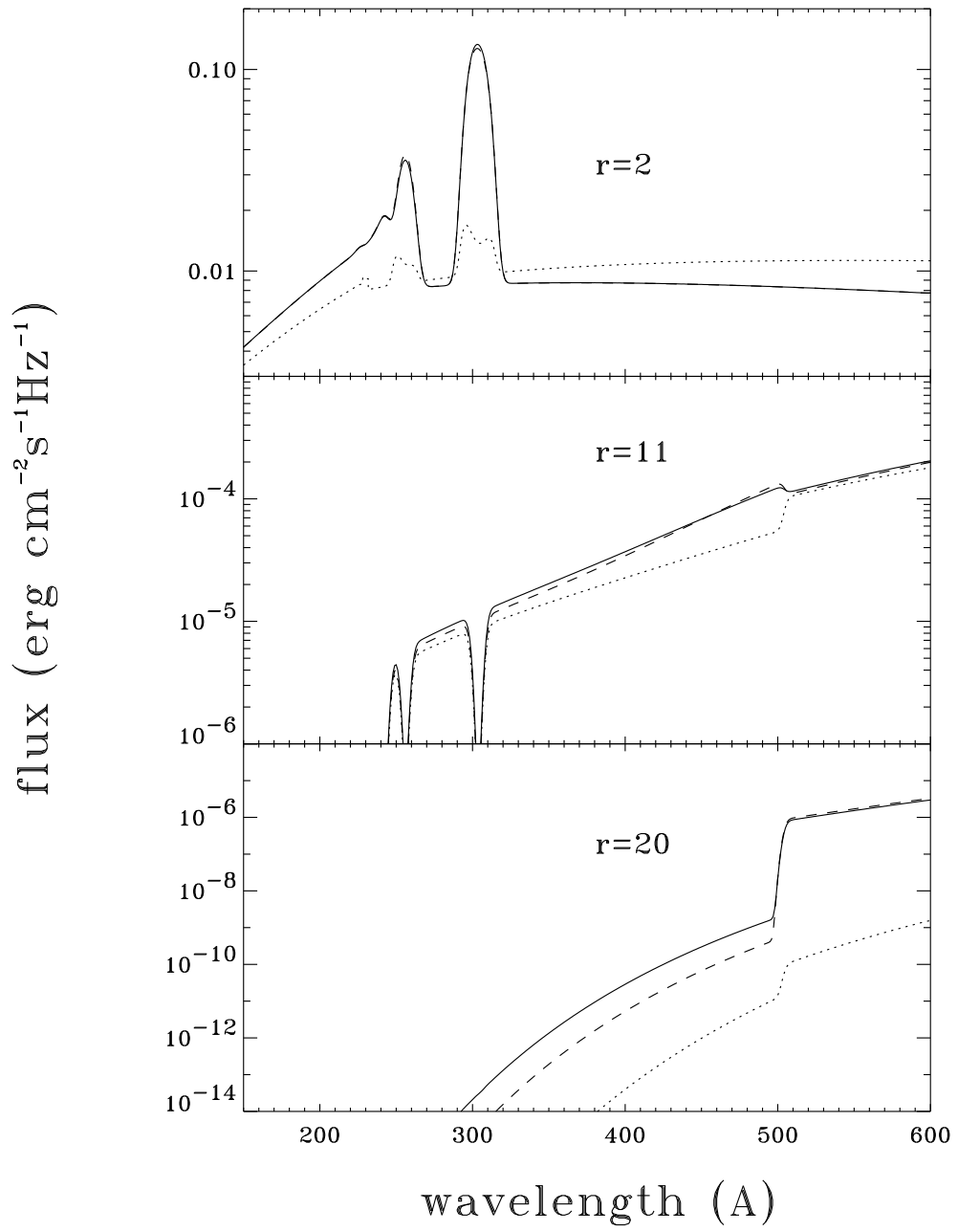


Fig. 6.— The same as in Fig. 5 for the EUV spectrum at the region of He II Lyman discontinuity ($\lambda = 227$ Å), and the He I ground-state discontinuity ($\lambda = 504$ Å).

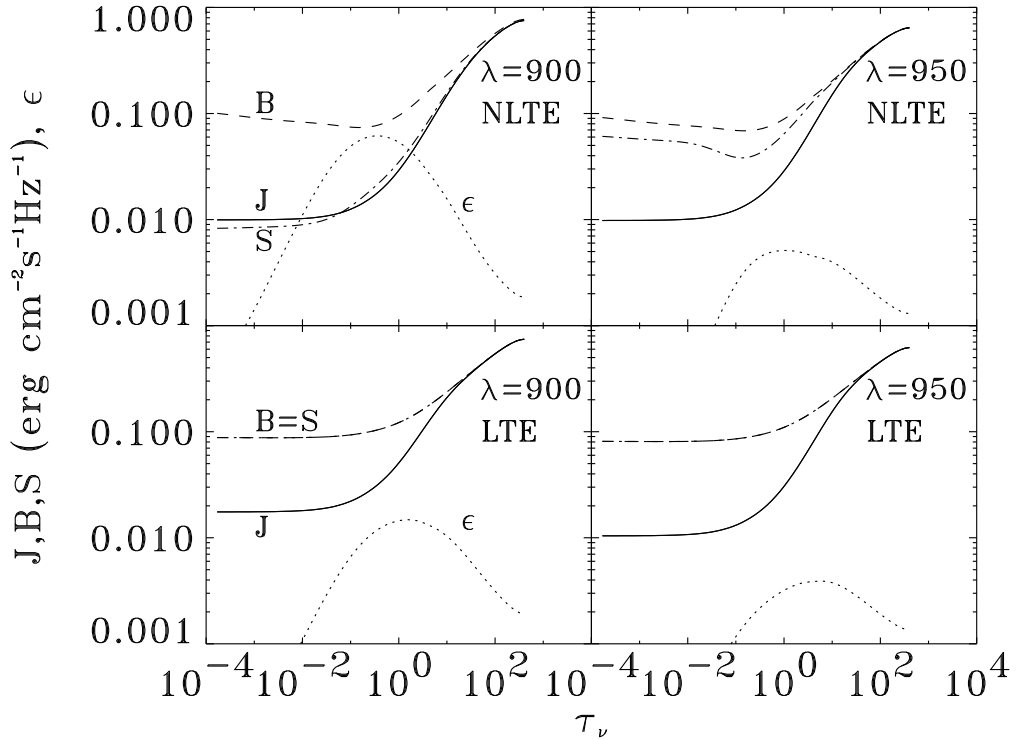


Fig. 7.— Plot of the mean intensity of radiation (full line, labeled J), the Planck function (dashed line, labeled B), the thermal source function (dot-dashed line, labeled S), and the thermal coupling parameter ϵ (dotted line), as a function of the monochromatic optical depth, for the model annulus at $r = 2$. The two upper panels are NLTE models; the two lower panels are LTE models. The left panels display the values for the blue side of the Lyman discontinuity ($\lambda = 900 \text{ \AA}$), and the right panels display the values for the red side of the Lyman discontinuity ($\lambda = 950 \text{ \AA}$).

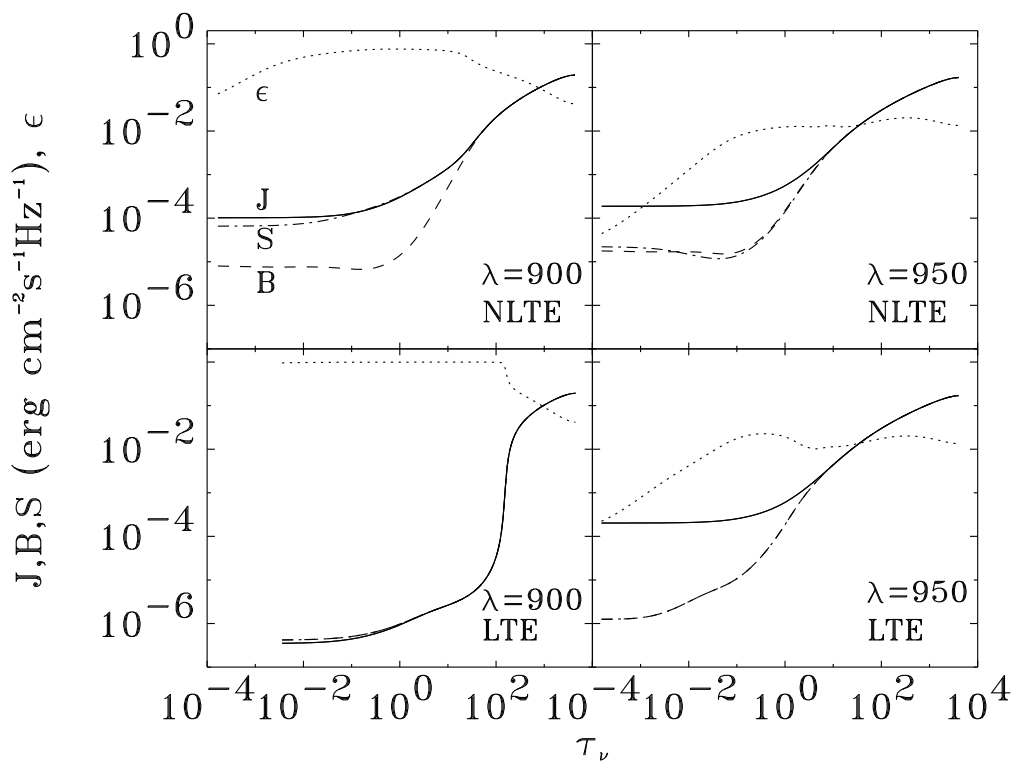


Fig. 8.— The same as in Fig. 7, but for the model annulus at $r = 20$.

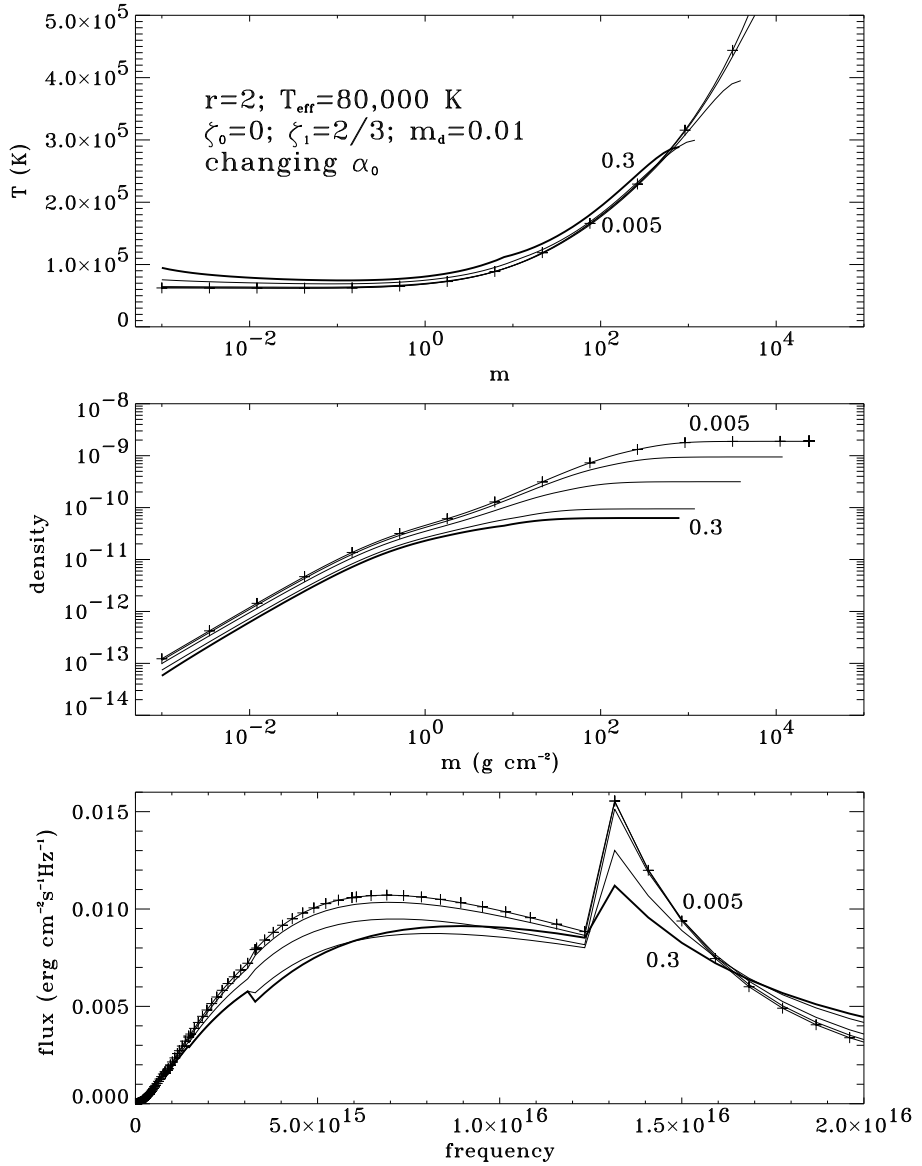


Fig. 9.— The effect of α_0 on the vertical structure and emergent flux for the model annulus at $r = 2$. Other basic parameters are the same as for the models displayed in Fig. 1, namely $\zeta_0 = 1$, $\zeta_1 = 1$, and $m_d = 0.01$. Upper panel: temperature; middle panel: mass density; and lower panel: emergent flux. The thick line corresponds to the highest α_0 , $\alpha_0 = 0.3$, the line with additional “+” signs to the lowest one, $\alpha_0 = 0.005$, and the curves in between to $\alpha_0 = 0.1$, 0.03 , and 0.01 . The curves for the two extreme values are labeled by the values of α_0 .

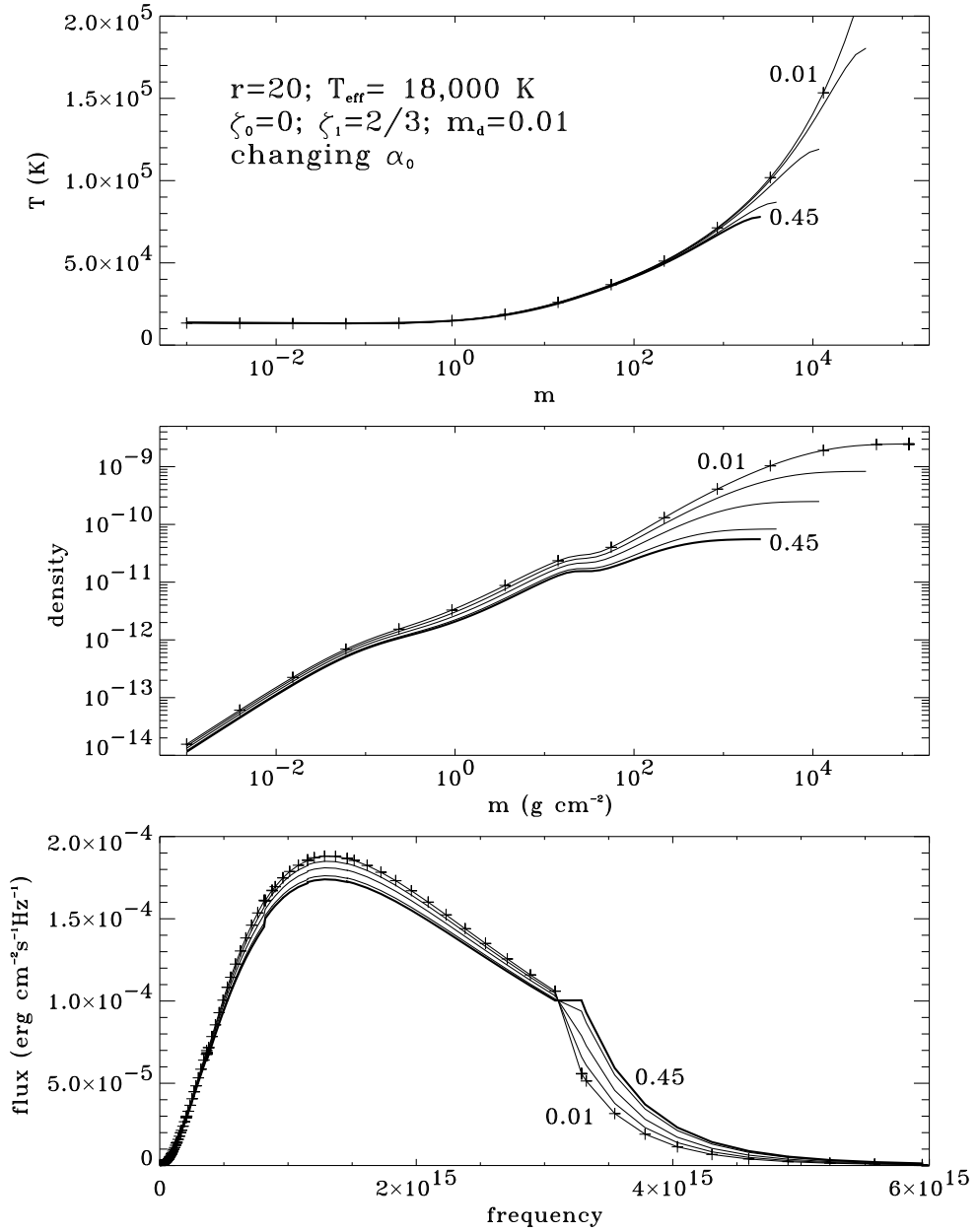


Fig. 10.— Analogous to Fig. 7, for the model annulus at $r = 20$; the adopted α_0 values are 0.45 (thick line), 0.3, 0.1, 0.03, and 0.01 (the line with additional “+” signs).

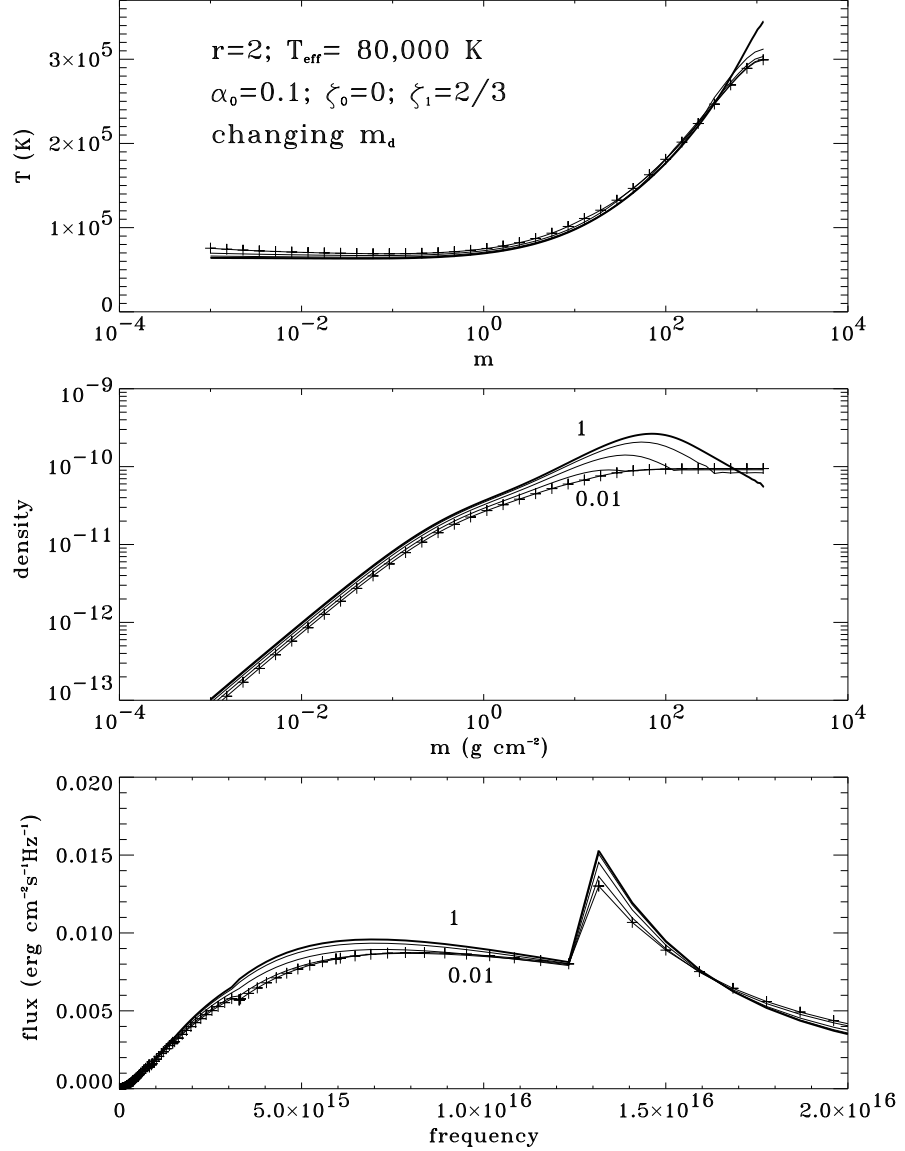


Fig. 11.— The effect of m_d (the division point between two different power laws of viscosity parameterization) on the vertical structure and emergent flux for the model annulus at $r = 2$. Other basic parameters are the same as for the models displayed in Fig. 1, namely $\zeta_0 = 1$, $\zeta_1 = 2/3$, and $\alpha_0 = 0.1$. The panels are arranged as in Fig. 7. The adopted values of m_d are: 1 (thick line); 0.3; 0.1; 0.03; and 0.01 (the line with additional “+” signs). The curves for the two extreme values are labeled by the values of m_d .

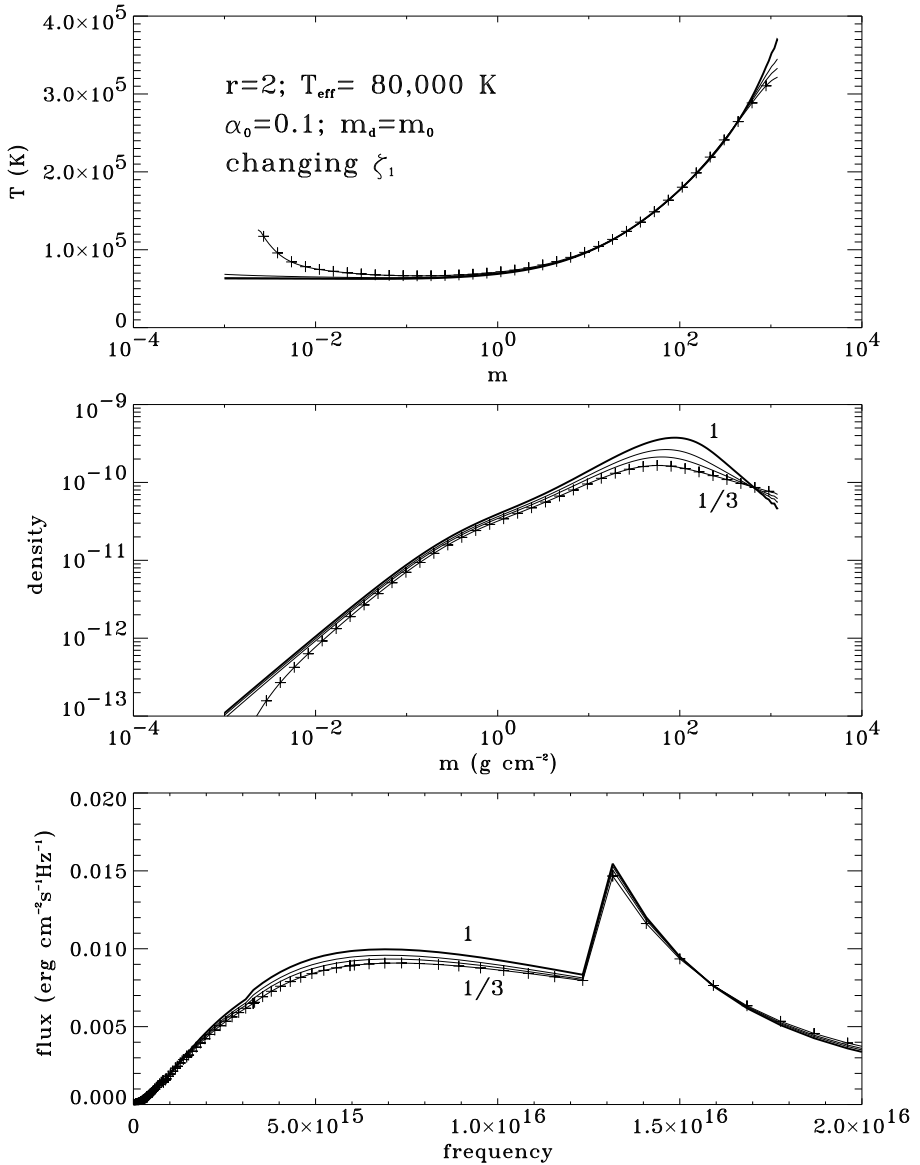


Fig. 12.— The effect of the power law exponent ζ_1 on the vertical structure and emergent flux for the model annulus at $r = 2$. Other basic parameters are $\alpha_0 = 0.1$, and $m_d = 1$ (i.e., no inner region of constant viscosity). The panels are arranged as in Fig. 7. The adopted values of ζ_1 are: 1 (thick line); 2/3; 1/2; and 1/3 (the line with additional “+” signs). The curves for the two extreme values are labeled by the values of ζ_1 .

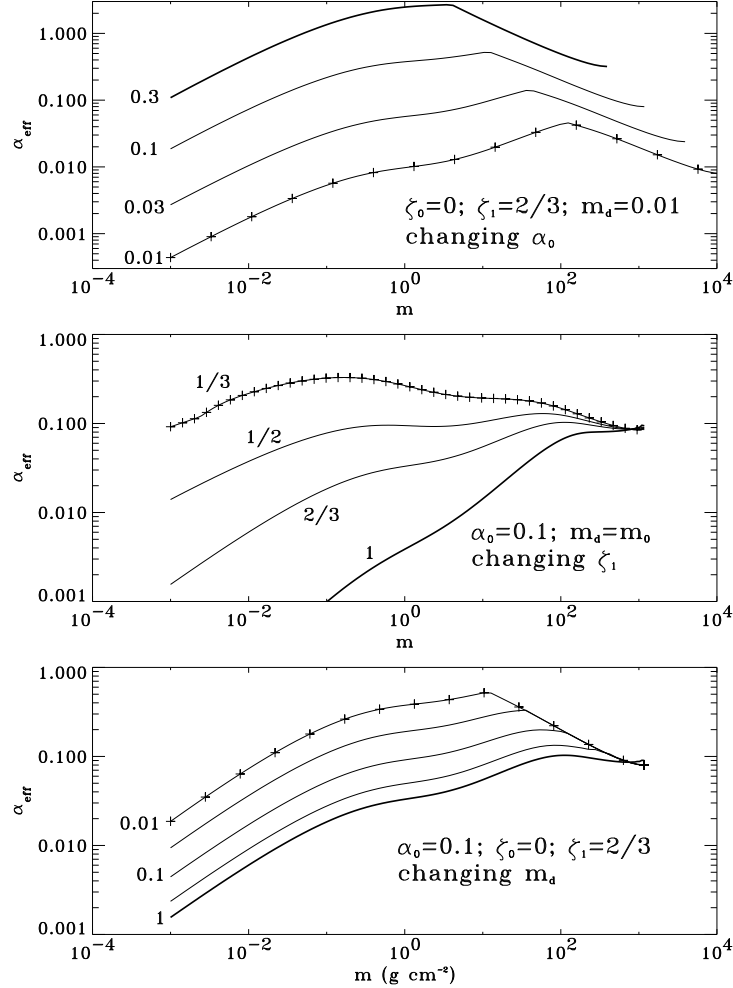


Fig. 13.— Plot of effective α -viscosity parameter that would yield the same value of kinematic viscosity in our models and in the α -parameterization of viscosity suggested by Dörrer et al. (1996). Upper panel – α_{eff} for the models displayed in Fig. 7, i.e., the models of the $r = 2$ annulus with $\zeta_0 = 0$, $\zeta_1 = 2/3$, and $m_d = 0.01$, and with various values of α_0 . The adopted values of α_0 are (from top to bottom): 0.3 (thick line), 0.1, 0.03 and 0.01 (the line with additional “+” signs). Middle panel – α_{eff} for the models displayed in Fig. 10, i.e., the models of the $r = 2$ annulus with $\alpha_0 = 0.1$, $m_d = 1$, and with various values of ζ_1 . The adopted values of ζ_1 are (from bottom to top): 1 (thick line); 2/3; 1/2; and 1/3 (the line with additional “+” signs). Lower panel – α_{eff} for the models displayed in Fig. 9, i.e., the models of the $r = 2$ annulus with $\alpha_0 = 0.1$, $\zeta_0 = 0$, $\zeta_1 = 2/3$, and with various values of the division depth m_d . The adopted values of m_d are (from bottom to top): 1 (thick line); 0.3; 0.1; 0.03; and 0.01 (the line with additional “+” signs).